Geothermics 88 (2020) 101908

Contents lists available at ScienceDirect

Geothermics

journal homepage: www.elsevier.com/locate/geothermics

CFD modelling of a thermal chimney for air-cooled condenser

Wenguang Li, Guopeng Yu, Daniele Zagaglia, Richard Green, Zhibin Yu*

School of Engineering, University of Glasgow, Glasgow, G12 8QQ, UK

ARTICLE INFO

Keywords:
Thermal performance
Thermal chimney
Nusselt number
Geothermal power plant
Conjugate heat transfer
Computational fluid dynamics

ABSTRACT

Thermal chimney driven/enhanced air-cooled condensers have increasingly found extensive applications in buildings, thermal and geothermal power plants. A small scale model of thermal chimney with rectangular cross-section of constant area was designed and one-row electrical heaters were installed to mimic the shell-and-tube heat exchanger, and simulations of conjugate heat transfer in the chimney were carried out by using computational fluid dynamics (CFD) software-ANSYS CFX at various heater nominal temperatures and 22.5 °C ambient temperature. The heat transfer models adopted include steady three-dimensional Reynolds-averaged Navier-Stokes equations and $k-\omega$ turbulence model as well as Boussinesq buoyancy assumption. The radiation effect from the heaters to the air was considered. The heater temperature profile was mapped by using forward-looking infrared camera and the air velocity in the chimney was measured by employing particle image velocimetry to validate CFD velocity fields. The measured temperature profile was modelled and involved into CFX as temperature boundary conditions. It was shown that the heaters can induce an air flow in the chimney to generate a cooling effect. As the heater nominal temperature increases from 80 °C to 170 °C, the chimney energy gain coefficient rises from 0.40 to 0.60, but saturated beyond 130 °C, the Reynolds number of the chimney is ranged in 2000–4000, while the Reynolds number of the heaters varies in 140–270, and the Nusselt number of the heaters is as low as 7.0-8.2. Flow separation can occur at lower than 130 °C. The radiation from the heaters makes a slightly more 1/3 contribution in the heat transfer. It is suggested that the primary heat exchanger/heater should operate at a temperature above 130 °C.

1. Introduction

Traditionally, chimneys are an architecture structure for initiating a hot air flow to discharge the smoke (hot air) out of a house/building. A chimney is composed of two elements, i.e. a heat source and a vertical duct. In the chimney, the air is hot, and its density is less than the air outside the chimney. Naturally, the air goes up in the chimney driven by the buoyancy generated by the difference in the air density inside and outside the chimney. Specially, the air velocity is so high that it can drive a small-sized wind turbine. At the entry to a chimney, air is in ambient temperature but with a certain velocity, thus can generate a cooling effect on a body with a temperature higher than the ambient temperature.

Basically, there are two types of chimney according to heat sources involved, namely solar chimney and residual heat driven chimney (natural draft air-cooled condenser). The cooling effect in solar chimneys has been used to carry out passive ventilation and building space air conditioning (Zhai et al., 2011; Lal et al., 2013; Abdallah et al., 2014; Park and Battaglia, 2015), and enhance natural draft cooling tower in thermal (Zandian and Ashjaee, 2013; Ghorbani et al., 2015) and geothermal (Zou et al., 2012; Hooman et al., 2017) power plants. The residual heat driven chimneys have been applied to remove residual heat in thermal power systems (Guan and Gurgenci, 2009; Zhao et al., 2015).

Existing combined power and freshwater production plants based on geothermal resources can be divided into three categories, namely flashed steam system, binary cycle system and total flow system, depending on brine temperature, dissolved solid content etc (Cortez et al., 1973; Austin et al., 1973; Austin and Lundberg, 1975). The total flow system is more efficient than the others (Smith, 1993; Smith and da Silva, 1994). For brines over 150 °C, the flashed steam system is usually applied with the mean total system efficiency of 12 % (Zarrouk and Moon, 2014). For brines less than 150 °C, however, the binary cycle system is utilized commonly (Chamorro et al., 2012).

A total flow energy conversion for a specific geothermal source with a capacity of 500 kW in Russia was developed with two-phase Pelton turbine (Trusov et al., 1995). A system combining electrical power and freshwater production from brines was proposed initially in (Yu and Yu, 2019) based on a liquid-dominated geothermal field in eastern Africa operated 100 − 250 °C. It was shown that the overall efficiency of the

* Corresponding author.
E-mail address: Zhibin.Yu@glasgow.ac.uk (Z. Yu).

https://doi.org/10.1016/j.geothermics.2020.101908
Received 25 March 2020; Received in revised form 17 May 2020; Accepted 30 June 2020

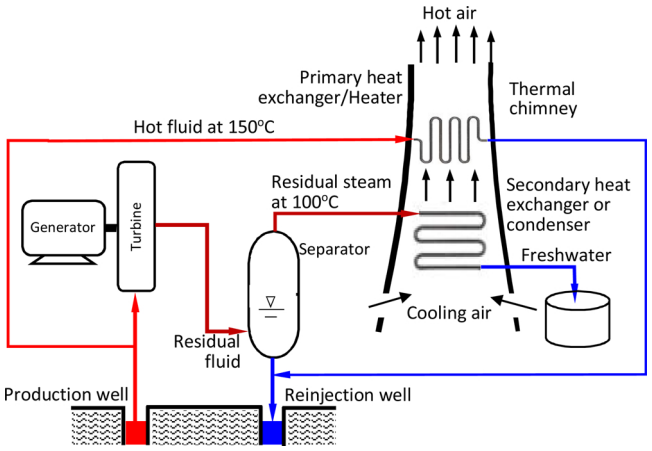

Fig. 1. A thermal chimney design concept to enhance freshwater yield from the residual fluid discharged by a two-phase flow turbine which extracts electric power from a hot fluid in a geothermal source at around 150 °C.

total flow system is comparable to the efficiencies of the steam cycle system and single-flashed cycle system. However, the freshwater yield harvested from the residual steam discharged by two-phase flow turbines in the former is 2.7 times higher than that in the latter.

To enhance freshwater yield, a thermal chimney design concept was initiated to intensify air cooling effect on the residual steam by using a residual heat driven chimney, as shown in Fig. 1. A stream of hot fluid discharged from the production well adds its heat to the air in the chimney with a primary heat exchanger/heater and the air body becomes hot. Eventually, the hot air flows out of the chimney due to the buoyancy effect. To maintain fluid continuity, the cold air is sucked into the chimney through the slots near bottom of the chimney and takes heat away from the secondary heat exchanger/condenser to allow the vapour in the steam to condensate, and a stream of freshwater will be produced.

To evaluate this concept, a series of CFD simulations was performed in (Ma et al., 2019) based on two-dimensional (2D) chimney model with emphasis on heat transfer-fluid flow interaction based on laminar and different turbulence models. It is shown that a thermal plume can be developed and its temperature keeps down but the velocity keeps increasing, and the flow eventually transits into turbulence. Single cylinder and a row of cylinders were explored, and an optimum dimensionless pitch of cylinders (pitch of two cylinders over cylinder diameter) is identified to be 1.75. This study has provided an insight into heat transfer in the thermal chimney. However, these simulations are 2D and three-dimensional (3D) effects in a real thermal chimney remain unclear, but also the thermal performance of the chimney has not been clarified so far.

There has been a certain amount of CFD heat transfer simulations on various real solar thermal chimneys (Pastohr et al., 2004; Maia et al., 2009; Ming et al., 2013; Fasel et al., 2013; Hassan et al., 2018; Jameei et al., 2019; Nasraoui et al., 2019). However, the solar thermal chimney differs in structure, function and heat exchanger arrangement from the thermal chimney proposed in the paper. 3D CFD heat transfer simulations on the thermal chimney shown in Fig. 2 are unavailable in the literature presently.

In the paper, a 3D thermal chimney test model was built, and the primary heat exchanger with a row of electrical heating cylinders was installed to mimic the tubes of shell-and-tube heat exchangers. The air in the chimney was heated with the heater row to mimic heating effect of the primary heat exchanger with hot fluid on the air. The natural convection heat transfer and fluid flow in the chimney were simulated in ANSYS 2019R2 CFX based on the $k-\omega$ turbulence model along with radiation effect at 80 − 170 °C heater nominal temperatures. The temperature uneven profile along the heater axis was taken into account in terms of empirical correlations based on our experimental data. The fluid and heat transfer models were validated by using existing Nusselt number correlations found in the literature regarding to single tube and tube banks. The flow field in the chimney was validated with our particle image velocimetry (PIV) measurements made in the mid-span plane cross the heaters at three heater nominal temperatures. The thermal performance and thermal fluid flow characteristics were clarified. Several issues such as turbulence model, effect of buoyancy on turbulence production and dissipation and energy balance analysis were argued. To exclude the influence of the secondary heat exchanger on the primary heat exchanger, the former was not involved in the chimney. The thermal performance and thermal fluid flow characteristics of the chimney with both the primary and secondary heat exchangers will be demonstrated in a forthcoming paper.

2. Thermal chimney test rig and computational models

2.1. Thermal chimney test rig

A thermal chimney with rectangular cross-section of constant area was designed and fabricated, as shown in Fig. 2(a) with primary dimensions. The chimney is composed of four 5 mm thick transparent acrylic sheets and supported by two frames made of aluminium. There is one row of holes in a pair of sheets to install 12 cylindrical electrical heaters with 16 mm dimeter(d) and 200 mm length. These heaters serve as the primary heat exchanger/hot fluid heater and were connected to an OMEGA™ PID (proportional integral derivative) controller to allow their heating surface temperature to be in a desirable value. The bottom row of holes for the secondary heat exchanager is ignored and not simulated. The horizontal cartridge heaters are evenly distributed with the optimal centre-to-centre distance 1.75d, which was determined based on 2D CFD heat transfer simulations in (Ma et al., 2019). And the chimney distances below and above the heaters are 32.5d and 12.5d respectively. The physical property constants of the air, acrylic sheet and aluminium at 25 °C are listed in Table 1.

In Fig. 2(b), a chimney with simplified frames is presented for CFD heat transfer simulations. In the chimney cavity, an inner air body is created, and then the chimney is enclosed with an outer air body above the floor. The outer air body size is as big as 930(width) × 600(depth) × 1800(height)mm in comparison with the volume of 300(width) × 190(depth) × 730(height)mm for the inner air body to fully contain the thermal boundary layer over the chimney. Initially, the 12 heaters were modelled as heat sources with an intensity, however, the convergent behaviour of simulation is poor, and a trial-error-method is needed to match a known experimental temperature in the heater surfaces, thus this process is quite time-consuming. Eventually, the heaters have to be removed from the geometrical model, instead their surfaces contacting with the inner air body, as shown in Fig. 2(c) became wall and were assigned with known experimental temperatures. In this way, the convergent behaviour was improved and computational effort declines significantly.

2.2. Computational models

Physically, the air flow in the thermal chimney shown in Fig. 2(b) is natural/free convection heat transfer with the radiation effect from the heaters to the air at low Reynolds number. The flow may be in separation, i.e. the thermal boundary layers can separate from the chimney walls when the heaters operate at a low surface temperature.

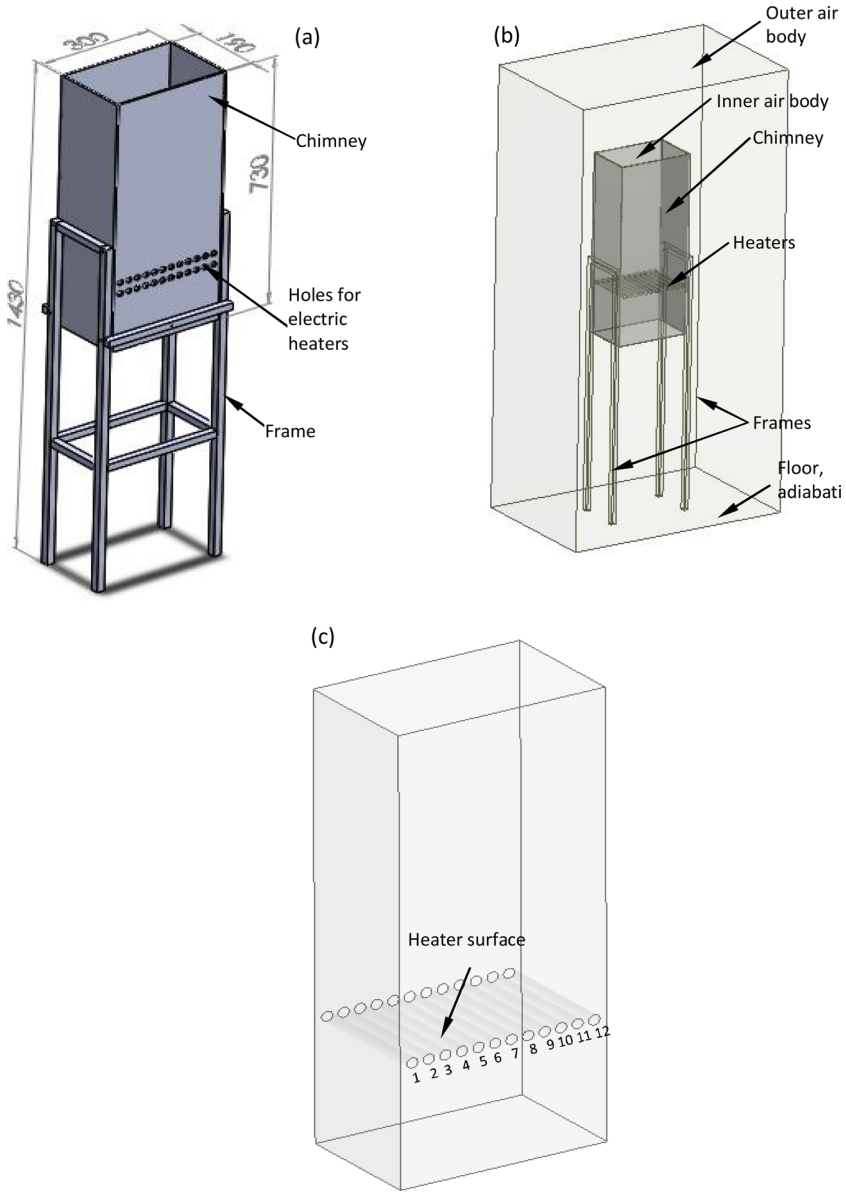

Fig. 2. A thermal chimney test model (a) and its computational geometrical model (b), in the latter, except solid domains such as chimney and frames, an outer air body with a size as big as 930 (width) × 600(depth) × 1800(height) mm and an inner air body with a volume of 300 (width) × 190(depth) × 730(height)mm, which is equal to the cavity volume of the chimney as shown in (c), are generated.

Bearing these facts in mind, ANSYS 2019R2 CFX was adopted to simulate the natural heat transfer in the thermal chimney test rig and predict its performance. For the air flows inside and around the chimney, their governing equations include the Reynolds-averaged Navier-Stokes (RANS) equations and thermal energy equation which are written as (ANSYS Inc, 2011)

Table 1
The physical property constants of air, acrylic sheet and aluminium at 25 °C.

Constant	Air(fluid)	Acrylic sheet(solid)	Aluminium(solid)
Density ρ_{ref}(kg/m^3)	1.185	1.19	2702
Specific heat capacity c_p (J/kg.K)	1004.4	1470	903
Thermal conductivity λ (W/m.K)	2.61×10^{-2}	0.19	237
Thermal expansivity β (1/K)	3.356×10^{-3}	N/A	
Dynamic viscosity μ (Pa.s)	1.831×10^{-5}		
Kinematic viscosity ν (m^2/s)	1.545×10^{-5}		
Absorption coefficient K (1/m)	0.01		
Refractive index n	1.0		

$$\begin{cases} \dfrac{\partial \rho}{\partial t} + \dfrac{\partial}{\partial x_j}(\rho u_j) = 0 \\ \dfrac{\partial(\rho u_i)}{\partial t} + \dfrac{\partial}{\partial x_j}(\rho u_i u_j) = -\dfrac{\partial p}{\partial x_i} + \dfrac{\partial}{x_j}(\tau_{ij} - \rho \overline{u_i' u_j'}) + s_m \\ \dfrac{\partial(\rho h_{tot})}{\partial t} - \dfrac{\partial p}{\partial t} + \dfrac{\partial}{\partial x_j}(\rho u_j h_{tot}) = \dfrac{\partial}{\partial x_j}\left(\lambda \dfrac{\partial T}{\partial x_j} - \rho \overline{u_j' h}\right) + \dfrac{\partial}{\partial x_j}[u_i(\tau_{ij} - \rho \overline{u_i' u_j'})] + s_e \end{cases} \quad (1)$$

where ρ is the density of air, u_i is an averaged velocity component of air, p is the static pressure of air, τ_{ij} is the molecular shear stress tensor of air flow, s_m is a source term in the momentum equations, λ is the conductivity of air, s_e is a source term in the thermal equation, h is the static enthalpy of air, h_{tot} is the mean total enthalpy of air, $h_{tot} = h + u_i u_i/2 + k$, k is the turbulent kinetic energy, $k = \overline{u_i'^2}/2$, u_i' is the fluctuating velocity component. The term $\partial[u_i(\tau_{ij} - \rho \overline{u_i' u_j'})]/\partial x_j$ in the thermal equation represents the internal heating effect by fluid viscosity, called viscous dissipation, and can be neglected due to the low air velocity in the chimney.

In the natural convection heat transfer in the thermal chimney test rig, buoyance effect can occur. Since the temperature rise (< 10 °C) is small when the air crosses the heaters in the chimney, the Boussinesq model is activated and the source term in the momentum equations is calculated with the following expression (ANSYS Inc, 2011)

$$s_m = -\rho_{ref} \beta (T - T_{ref}) g \quad (2)$$

where T_{ref} is the reference ambient temperature, $T_{ref} = 25$ °C, ρ_{ref} is the air density at T_{ref}, β is the thermal expansivity of air, g is the gravity acceleration, $g = 9.81$ m/s^2, ρ_{ref}, β and λ values are listed in Table 1.

The term $-\rho \overline{u_i' u_j'}$ in Eq. (1) is due to turbulent velocity fluctuation, called the Reynolds stresses, which need additional methods for modelling. To reduce computational effort and properly handle low Reynolds number and flow separation effects, the eddy viscosity based $k - \omega$ turbulence model was adopted in the thermal chimney. In the model, the Reynolds stresses $-\rho \overline{u_i' u_j'}$ are expressed by the mean velocity gradients and the eddy or turbulent viscosity as follows (ANSYS Inc, 2011)

$$-\rho \overline{u_i' u_j'} = \mu_t \left(\frac{\partial u_i}{\partial x_j} + \frac{\partial u_j}{\partial x_i}\right) - \frac{2}{3}\delta_{ij}\left(\rho k + \mu_t \frac{\partial u_k}{\partial x_k}\right) \quad (3)$$

where μ_t is the turbulent viscosity, calculated by using the turbulent kinetic energy k and turbulent frequency ω via $\mu_t = \rho k/\omega$. The equations for solving k and ω are written as the following (ANSYS Inc, 2011)

$$\begin{cases} \dfrac{\partial(\rho k)}{\partial t} + \dfrac{\partial}{\partial x_j}(\rho u_j k) = \dfrac{\partial}{\partial x_j}\left[\left(\mu + \dfrac{\mu_t}{\sigma_k}\right)\dfrac{\partial k}{\partial x_j}\right] + P_k - \beta' \rho k \omega + P_{kb} \\ \dfrac{\partial(\rho \omega)}{\partial t} + \dfrac{\partial}{\partial x_j}(\rho u_j \omega) = \dfrac{\partial}{\partial x_j}\left[\left(\mu + \dfrac{\mu_t}{\sigma_\omega}\right)\dfrac{\partial \omega}{\partial x_j}\right] + \alpha \dfrac{\omega}{k} P_k - \beta \rho \omega^2 + P_{\omega b} \end{cases} \quad (4)$$

where the model constants are given by $\beta' = 0.09$, $\alpha = 5/9$, $\beta = 0.075$ and $\sigma_k = \sigma_\omega = 2$. P_k is the turbulence production term because of viscous forces, and modelled by the mean velocity gradients and expressed as (ANSYS Inc, 2011)

$$P_k = \mu_t \left(\frac{\partial u_i}{\partial x_j} + \frac{\partial u_j}{\partial x_i}\right)\frac{\partial u_i}{\partial x_j} - \frac{2}{3}\frac{\partial u_k}{\partial x_k}\left(3\mu_t \frac{\partial u_k}{\partial x_k} + \rho k\right) \quad (5)$$

The term P_{kb} is the buoyancy production in the k equation, and for the Boussinesq model, the term is expressed as $P_{kb} = \rho \beta g_i (\mu_t/\rho \sigma_b)(\partial T/\partial x_i)$, where σ_b is the turbulence Schmidt number, $\sigma_b = 0.9$. The buoyancy production term $P_{\omega b}$ in the ω equation reads as $P_{\omega b} = \omega[(\alpha + 1)C_3 max(P_{\omega b}, 0) - P_{kb}]/k$, C_3 is turbulence dissipation coefficient, for the Boussinesq buoyancy model, $C_3 = 1$.

$-\rho \overline{u_j' h}$ in Eq.(1) is the term, called Reynolds flux, which needs to be modelled. Based on eddy diffusivity hypothesis, the h flux is linearly linked to the mean h gradient, i.e. $-\rho \overline{u_j' h} = (\mu_t/Pr_t)(\partial h/\partial x_i)$, Pr_t is the turbulent Prandtl number, $Pr_t = 0.85$. Since the air velocity in the thermal chimney is low, three terms P_{kb}, $P_{\omega b}$ and $-\rho \overline{u_j' h}$ are not considered in the simulations herein.

Because of the limitation in our computational resources, the boundary layer flows over the heaters and chimney walls are not simulated physically by generating very fine mesh near these walls. Instead, the automatic near-wall treatment in the $k - \omega$ turbulence model was enforced in the simulations. This treatment includes two innovative measures in coarse meshes: one is scalable wall function at a high Reynolds number, and one is respectively blended analytical fractional velocity and ω expressions between log-law outer layer and liner-law viscous sublayer at a low Reynolds number.

In the scalable wall function, a turbulent kinetic energy based frictional velocity is defined to overcome the singularity in the log-law at boundary layer flow separation points, and all the expressions for the function are as follows (ANSYS Inc, 2011)

$$u^* = C_\mu^{1/4} k^{1/2},\ y^* = \max(\rho u^* \Delta y/\mu, 11.06),\ u_\tau = \frac{u_t}{\frac{1}{\kappa} ln y^* + C},\ \tau_w = \rho u^* u_\tau \quad (6)$$

where the constants $C_\mu = 0.09$, $\kappa = 0.41$ and $C = 5.0$, u_t is the known velocity in parallel to the wall at a distance of Δy from the wall, u_τ is the frictional velocity, τ_w is the wall shear stress. 11.06 is the value of y^* at the interaction between the logarithmic and the linear near wall velocity profiles.

The blended analytical fractional velocity and ω expressions permit the viscous sublayer can be handled analytically at low Reynolds numbers even in coarse grids rather than by employing a very fine mesh near the wall under heat transfer conditions (ANSYS Inc, 2011).

The heat flux at the wall is modelled by using a universal temperature profile across the viscous sublayer and logarithmic-law region as the following (ANSYS Inc, 2011)

$$\begin{cases} T^+ = Pry^* e^{-\Gamma} + (0.1 ln y^* + \beta) e^{-1/\Gamma} \\ \beta = (3.85 Pr^{1/3} - 1.3) + 0.1 ln Pr \\ \Gamma = \dfrac{0.01(Pry^*)^4}{1 + 5Pr^3 y^*},\ T^+ = \dfrac{\rho c_p u^* (T_w - T_f)}{q_w},\ Pr = \mu c_p/\lambda \end{cases} \quad (7)$$

where T^+ is the dimensionless temperature and Pr is Prandtl number, T_w and q_w are the temperature on the wall and heat flux through the wall, T_f is the near wall fluid temperature, c_p and λ are the heat capacity at constant pressure and thermal conductivity of air, respectively.

Except the natural convection heat transfer, there are radiative transfer effects in the thermal chimney from the heaters to the air and chimney walls as well as the walls to the air outside the chimney. The radiation from the heaters to the air in the chimney can be more dominant than these from the heaters to the chimney walls and the walls to the air outside the chimney. Since the frequency spectrum information of the radiation and scattering effect in the air are unknown, these two effects have to be neglected. Finally, the grey radiative transfer equation can be written as (ANSYS Inc, 2011)

$$\frac{dI(\boldsymbol{r}, \boldsymbol{s})}{ds} = -KI(\boldsymbol{r}, \boldsymbol{s}) \quad (8)$$

where the air in the chimney is regarded as participating medium with an absorption coefficient K, I is the radiation intensity in the air, and is dependent on position $\boldsymbol{r}$ and direction $\boldsymbol{s}$. Eq.(8) is solved by using the Monte Carlo method.

Conduction heat transfer takes place in the solid domains including the chimney walls and frames, and it is suggested that conjugate heat transfer should happen in the chimney. Within these stationary solid domains, the conservation of energy equation for the conduction heat transfer is written as (ANSYS Inc, 2011)

$$\frac{\partial(\rho h)}{\partial t} = \nabla \bullet (\lambda \nabla T) + s_e \quad (9)$$

Table 2
Element size, number of elements, aspect ratio, and chimney thermal gain coefficient predicted.

Mesh name		Mesh1	Mesh2	Mesh3
Mesh type	Inner air body Outer air body Chimney Frames	Hexahedral Tetrahedral		
Element size (mm)		7.5	5.75	5.0
Number of elements		1,112,568	1,650,611	2,253,708
Aspect ratio	Min	1.16	1.13	1.16
	Max	13.86	14.94	15.96
	Average	2.35	2.03	2.02
	Standard deviation	0.86	0.57	0.56
Energy gain coefficient η_{th}	T_{hn} = 90°C	0.4409	0.4522	0.4488
	T_{hn} = 110°C	0.5415	0.5400	0.5327
	T_{hn} = 130°C	0.5693	0.5837	0.5816
	T_{hn} = 150°C	0.5919	0.6022	0.5872
	T_{hn} = 170°C	0.5930	0.6045	0.6059

where h, ρ and λ are the enthalpy, density and thermal conductivity of the solids, respectively; s_e is the source term, and $s_e = 0$ for the thermal chimney. To maintain the conjugate heat transfer, the surfaces of the solid domains contacting with the air body are set up to be the heat transfer interfaces across which the radiative and conductive heat fluxes are kept conservative. Further, the solid domains are not considered participating medium, and the radiative effect of the heaters on the heat transfer in the solid domains is ignored in the paper.

2.3. Boundary conditions

Proper boundary conditions are required for conjugate heat transfer simulations in the thermal chimney. Since the solid domains are surrounded by two air bodies and the ground floor, the domains are mostly subject to solid-fluid interfaces where the fluxes remain unchanged except four surfaces of the frames which contact with the ground floor. On these surfaces, the adiabatic wall boundary condition is held.

Similarly, in the outer air body, the surface contacting with the floor is adiabatic wall and with no-slip boundary condition. Five exposed surfaces in the outer air body are assigned to be zero relative opening pressure above 1 atm reference pressure, 22.5 °C opening temperature, 5 % turbulence intensity and blackbody radiation to the surrounding air based on the local and environmental temperatures. The air crosses these five surfaces in the normal directions of them.

Most surfaces of the inner air body are either solid-fluid or fluid-fluid interfaces, however, twelve surfaces in them are the walls which contact with twelve heaters, see Fig. 2(c). These walls are subject to no-slip velocity boundary condition, heat transfer and thermal radiation conditions. For the thermal radiation condition, the emissivity ε and diffusion fraction of the walls should be provided. The surfaces of 12 heaters have been painted with a black paint to facilitate velocity measurements by PIV, thus they are opaque with $\varepsilon = 1$ emissivity. Under this condition, the diffusion fraction is set to be zero. Eventually, the radiation intensity emitted from these surfaces is determined with (ANSYS Inc, 2011)

$$I_{ra} = \varepsilon I_b(T) = \varepsilon n^2 \sigma T_h^4 \tag{10}$$

where $I_b(T)$ is the blackbody emission intensity, n is the air refractive index, $n = 1.0$, σ is the Stefan-Boltzmann constant, T_h is the local temperature on a heater surface.

The heat transfer condition requires to specify a temperature for the heater surfaces. To identify the temperature profile on the surfaces of 12 heaters, the surfaces of the heaters were imaged by using a forward-looking infrared (FLIR) camera at 120 °C nominal temperature monitored by the thermal coupling fixed on the surface of heater 6, as shown in Fig. A1 in Appendix A. It turned out that the temperature on the heater surfaces are not isothermal, but also varies from one heater to another. This fact suggests that assigning a constant uniform temperature to all the heaters is improper. Thus, further three experiments were performed by employing the camera at 120, 130 and 140 °C nominal temperatures under allowable working conditions for the camera. After the experimental data were processed, three analytical empirical equations such as Eqs. (23)–(25) in Appendix A were developed to specify the temperature profiles along the heater axis and across 12 heaters as temperature boundary condition by using CFX expression language (CEL) in CFX-Pre.

In the simulations, the high-resolution scheme and 2^{nd}-order scheme were applied in the convection and diffusion terms in Eqs. (1), (4) and (9), respectively. The maximum iteration number is 1000 and residual target for all the variable is 10^{-6} in terms of root-mean-square error. In the Monte Carlo method, the target coarsening rate is 16, small coarse grid size is 2×10^4, and recorded number of histories is 2×10^5. The coupling between radiation and thermal computation takes place at every 20 iteration intervals.

2.4. Mesh size independence and velocity validation

To examine mesh size independence, three meshes, Mesh1, Mesh2 and Mesh3, are created in terms of 8GB RAM desktop. The information about mesh/element size, number of elements, element aspect ratio, and energy gain coefficient predicted are listed in Table 2. The chimney energy gain coefficient is defined as the ratio of the air energy increase between the chimney inlet and outlet to the thermal energy input from the heaters, namely

$$\eta_{th} = \frac{m_f c_p (T_{f2} - T_{f1})}{\sum_{i=1}^{i=12} (q_{ri} + q_{ci}) A_{hi}} \tag{11}$$

where m_f is air mass flow rate through the chimney inlet or outlet, T_{f1} and T_{f2} are the air temperatures at the chimney inlet and outlet, respectively; A_{hi} is the total area of the surfaces of heater i exposed to the inner air body, $A_{hi} = 9.55 \times 10^{-3}$ m^2, q_{ri} is the wall radiative heat flux through the surface of heater i, q_{ci} is the wall convective heat flux across the surface of heater i. Parameters m_f, T_{f1}, T_{f2}, q_{ri} and q_{ci} are extracted from CFD simulation result files. Note that $1 - \eta_{th}$ should be the chimney energy loss coefficient through its side walls and inlet.

In general, Mesh1 results in a lower energy gain coefficient than Mesh2 and Mesh3 do, especially at low nominal heater temperature due to overestimated wall convective heat fluxes. Regarding to Mesh2 and Mesh3, the energy gain coefficient exhibits a variation as little as less 0.01 when the mesh is switched to Mesh3 from Mesh2. Thus, the results at Mesh2 are redeemed mesh-size-independent and will be present in the following sections.

To validate the velocity profile, PIV measurements were taken place in the mid-span plane across the heaters in the chimney at the heater nominal temperatures T_{hn} = 80, 120, 160°C, as shown in Fig. B1 in Appendix B. It was confirmed that the errors in the mean velocity between PIV and CFD at the nominal temperatures 80,120,160°C are in a range of (-30 ~ +2)% based on Table B1 in Appendix B.

3. Results

3.1. Overall thermal performance

Overall thermal performance for the thermal chimney includes mean input heat fluxes, mean heater temperature, mean air velocities at the chimney inlet and outlet, air mass flow rate through the chimney, various mean air temperatures and air temperature rise across the chimney, air energy gain coefficient of the chimney. These performance variables are plotted in Fig. 3 in terms of heater nominal temperature T_{hn}.

In Fig. 3(a), the mean air velocities at the inlet and outlet, u_{in} and

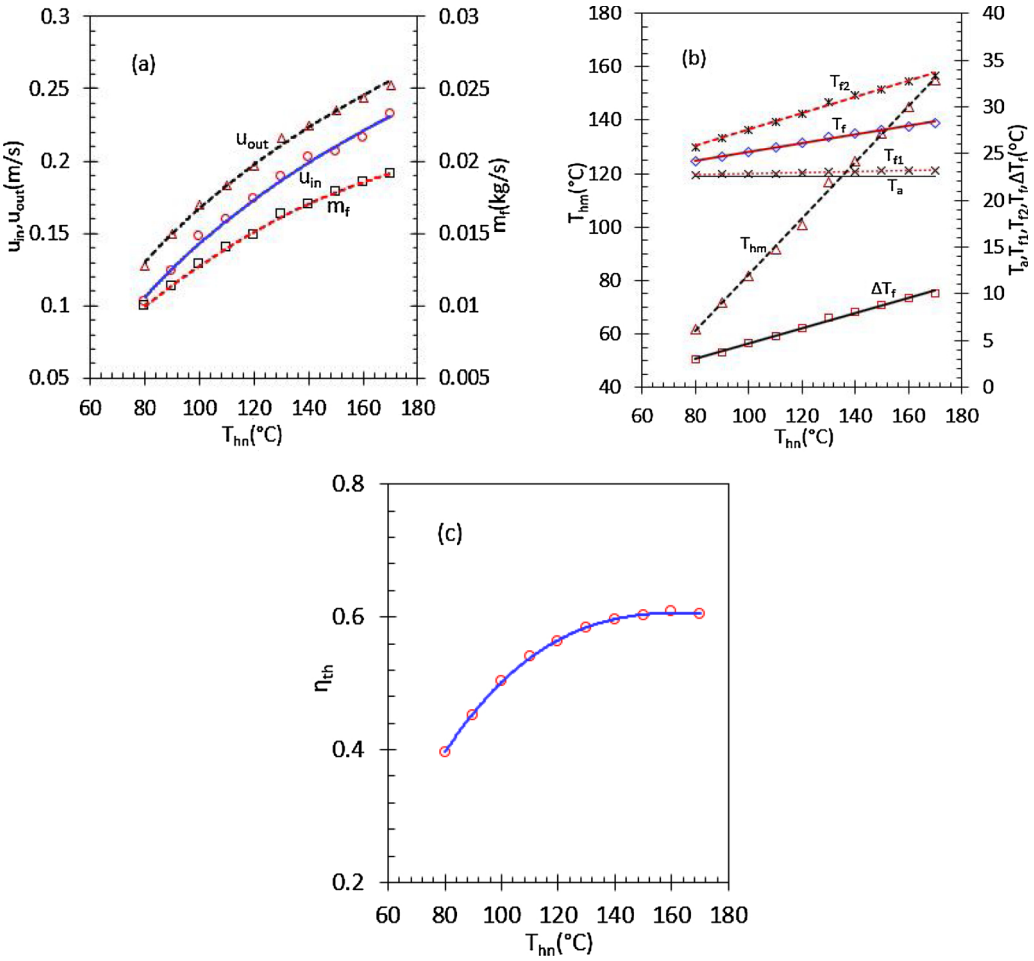

Fig. 3. The overall thermal performance of the thermal chimney in terms of heater nominal temperature, (a) mean air velocity at the chimney inlet and outlet, and air mass flow rate through the chimney, (b) ambient temperature, mean heater temperature, mean air temperatures at the chimney outlet and outlet, mean air temperature in the chimney and temperature rise across the chimney, and (c) air energy gain coefficient.

u_{out}, as well as the air mass flow rate m_f all steadily rise with increasing T_{hn} due to gradually intensified buoyancy effect. Since the air in the chimney is heated when it passes through the heaters, the air velocity at the outlet is higher than at the inlet, the difference between u_{in} and u_{out} implies the reduction in the density of air through the chimney. The air mass flow rate m_f is augmented by increasing T_{hn}, particularly the m_f curve resembles to the u_{in} and u_{out} curves.

In Fig. 3(b), the ambient temperature T_a is always in a constant of 22.5°C. The mean air temperature at the chimney inlet T_{f1} is linearly increased with T_{hn} but also slightly higher (by 0.8 °C in maximum) than T_a caused from the radiation effect of the heaters.

The mean air temperature at the chimney outlet T_{f2} varies with T_{hn} in a similar manner to T_{f1} but with a larger slope. It can be higher by (3.2–10.0) °C than T_a, depending on T_{hn}, specially, the higher the T_{hn}, the larger the difference $T_{f2} - T_a$.

The mean air fluid temperature in the chimney T_f is defined as the arithmetic mean of T_{f1} and T_{f2}, i.e.

$$T_f = 0.5(T_{f1} + T_{f2}) \tag{12}$$

Obviously, the T_f profile is in between of both T_{f1} and T_{f2}.

The air temperature rise ΔT_f can be correlated to T_{hn} linearly as well. To obtain a noticeable ΔT_f, T_{hn} should be higher than 100 °C at least.

Because the surface temperature is non-uniform axially along the heater, but also varies from one heater to another as shown in Figs. A1–A3, the mean heater surface temperature T_{hm} should be lower than the heater nominal temperature T_{hn}. In Fig. 3(b), a linear relationship between T_{hm} and T_{hn} is exhibited. The difference of T_{hm} from T_{hn} is narrowed with increasing T_{hn}, for example, a −20 °C difference at T_{hn} = 80 °C has been shrunken to a -10 °C difference at T_{hn} = 170 °C.

In Fig. 3(c), the energy gain coefficient η_{th} becomes better and better with increasing T_{hn} until 130 °C; beyond that temperature η_{th} gets saturated constantly and ends up with the best energy gain coefficient of 0.6 at $T_{hn} \geq$ 160 °C. In terms of η_{th}, the heater nominal temperature should be ≥ 130 °C at least.

3.2. Heat transfer characteristics

The heat transfer characteristics in the chimney is illustrated in Fig. 4, which include mean heat fluxes and Nusselt numbers. There exist two heat fluxes across the surfaces of a heater to heat the air in the chimney, one is the wall radiative heat flux q_r and one is the wall convective heat flux q_c.

In Fig. 4(a), the total mean wall heat flux $q_r + q_c$, mean convective heat flux q_c, and the ratio $q_c/(q_r + q_c)$ are illustrated versus T_{hn}. $q_r + q_c$ rises rapidly in a continuously enlarged slope with increasing T_{hn} in comparison with q_c, suggesting a steadily declined convection heat transfer as T_{hn} ascends. As a result, $q_c/(q_r + q_c)$ is slightly decreased towards 0.62 at a higher T_{hn} from 0.64 at a lower T_{hn}. Whatever the ratio is, the convection heat transfer is always more dominant than the radiative heat transfer in the thermal chimney in the range of heater nominal temperature considered in the paper.

In Fig. 4(b), mean convection Nusselt number *Nuc*, radiation equivalent Nusselt number *Nur*, Grashof number *Gr* and Rayleigh number *Ra* are demonstrated in terms of T_{hn}. Following (Shati et al.,

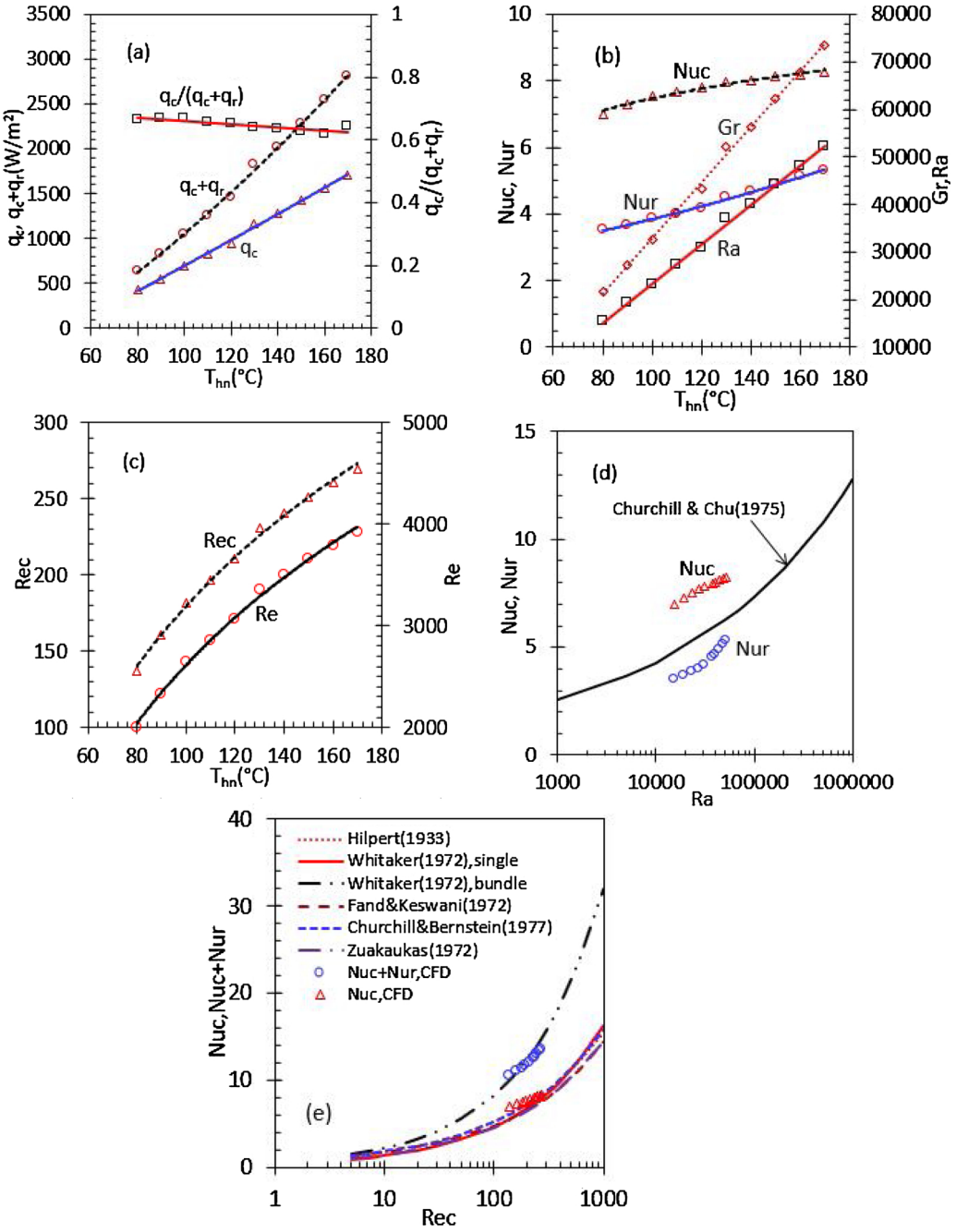

Fig. 4. The heat transfer characteristics of the thermal chimney, (a) convective heat flux q_c, and total heat flux $q_c + q_r$ as a function of nominal heater temperature T_{hn}, where q_r is radiative heat flux, and the ratio $q_c/(q_c + q_r)$ across the heater surfaces, (b) convection Nusselt number *Nuc*, radiation equivalent Nusselt number *Nur*, Grashof number *Gr* and Rayleigh number *Ra* in terms of T_{hn}, (c) heater Reynolds number *Rec* and chimney Reynolds number *Re* vs T_{hn}, (d) *Nuc* and *Nur* are plotted with *Ra*, and (e) *Nuc* and *Nuc* + *Nur* against.*Rec*.

2012; Saravanan and Sivaraj, 2013), both *Nuc* and *Nur* are calculated respectively by using q_c and q_r with the following expressions

$$\begin{cases} Nuc = \dfrac{1}{N}\sum_{i=1}^{N} \dfrac{q_{ci} d}{\lambda (T_{hmi} - T_f)} \\ Nur = \dfrac{1}{N}\sum_{i=1}^{N} \dfrac{q_{ri} d}{\lambda (T_{hmi} - T_f)} \end{cases} \tag{13}$$

where q_{ci} and q_{ri} are the mean convection and radiation heat fluxes of heater i, T_{hmi} is the mean temperature of heater i, d is the heater outer diameter, d = 16 mm, N is the number of heaters totally, N = 12. Additionally, mean *Gr* and *Ra* are estimated by the following expressions

$$Gr = \frac{g\beta (T_{hm} - T_f) d^3}{\nu^2}, \; R_a = GrPr \tag{14}$$

where ν is the air kinematic viscosity, $\nu = 1.545 \times 10^{-5}$ m^2/s, *Pr* is the air Prandtl number.

In that figure, both *Nuc* and *Nur*, especially *Nur*, arise with increasing T_{hn}, especially *Nuc* is more dominant in comparison with *Nur*. *Gr* and *Ra* are largely dependent on T_{hn}, and exhibit a linear relationship with T_{hn}.

In Fig. 4(c), the heater Reynolds number Re_c and chimney Reynolds number *Re* are shown, which are defined as follows

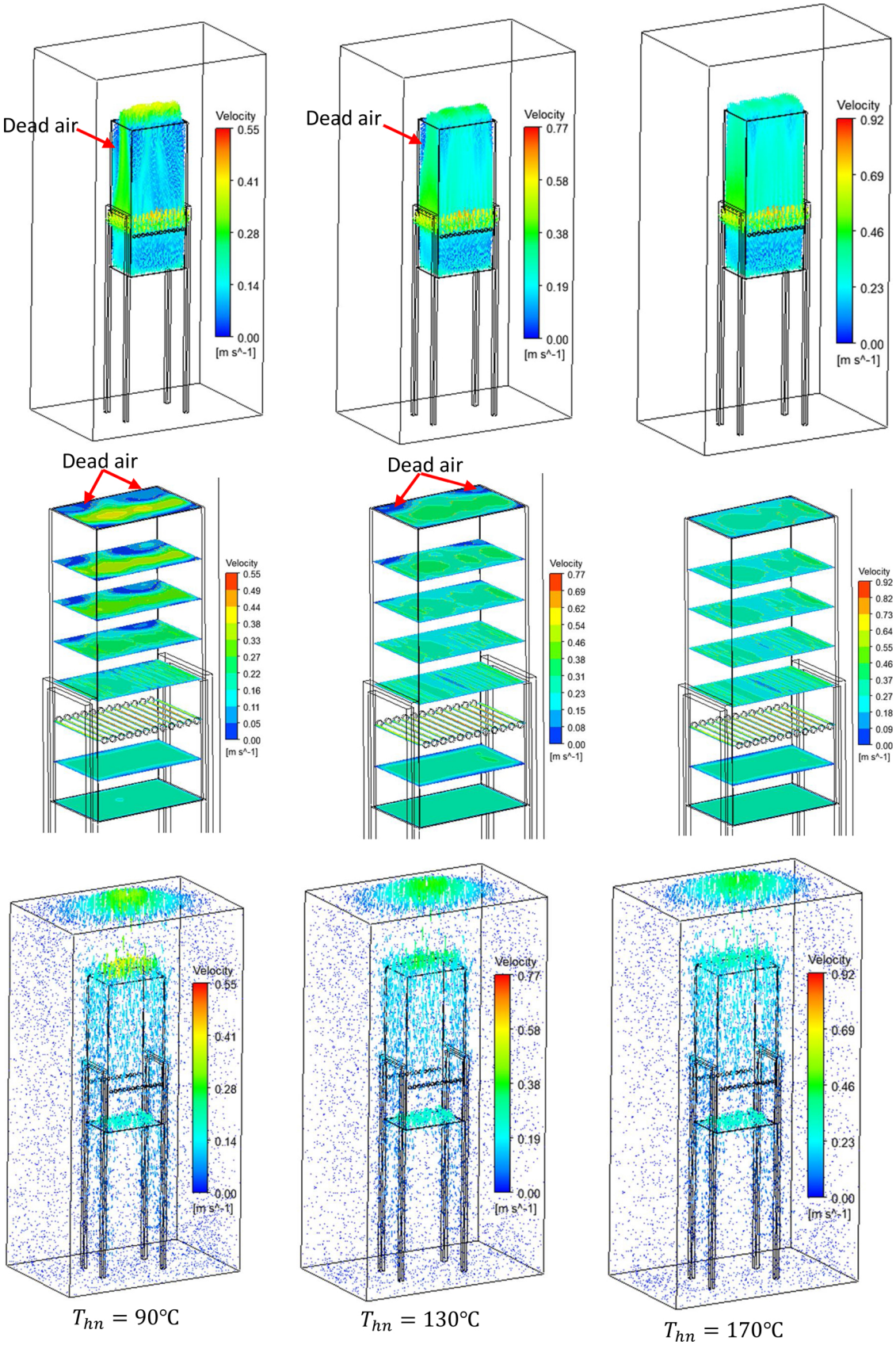

Fig. 5. The air velocity vectors inside the chimney (top row), velocity contours in eight cross-sections (middle row) and velocity vectors outside the chimney (bottom row) at three heater nominal temperatures $T_{hn} = 90,\ 130,\ 170°C$, respectively.

$$Re_c = \frac{u_f d}{\nu},\ Re = \frac{u_f d_h}{\nu},\ u_f = \frac{1}{2}(u_{in} + u_{out}),\ d_h = \frac{4ab}{2(a+b)} \tag{15}$$

where u_f is the air characteristic velocity, d_h is the hydraulic diameter of the chimney, a and b are the width and depth of the chimney inner cross-section, $a = 300$ mm, $b = 190$ mm. It is indicated that Re_c and Re increase with T_{hn}, however, they are confined in the ranges of [140,270] and [2000,4000], respectively. This fact suggests that the air flow in the chimney is in turbulence at low Reynolds number.

In Fig. 4(d), the heat transfer around the heaters are considered natural convection heat transfer in large enough space, and *Nuc* and *Nur* are plotted in terms of R_a. In that figure, *Nuc* for natural convection from a horizontal cylinder determined by using empirical correlation in (Churchill and Chu, 1975) is also present, which reads as

$$Nuc = \sqrt{0.60 + 0.387\left\{\frac{Ra}{[1 + (0.559/Pr)^{9/16}]^{16/6}}\right\}^{1/6}} \tag{16}$$

Obviously, *Nuc* in the paper is higher than *Nuc* from the correlation. This implies that the Nusselt number in the natural convection heat transfer from single horizontal cylinder is improper to the case where a horizontal hot cylinder row is placed in the chimney. *Nuc* should not be treated as a result of natural convection heat transfer over a single cylinder in infinite space of air.

In Fig. 4(e), *Nuc* and *Nur* + *Nuc* are illustrated as a function of Re_c and compared with those predicted with six empirical correlations of *Nuc* for flows crossing a single hot cylinder or cylinder bundle. A correlation of Nusselt number for experimental data of convection heart transfer when air flow crosses a heated single cylinder is expressed as follows (Hilpert, 1933)

$$Nuc = 0.615Re_c^{0.466},\ Re_c \in [40,4000] \tag{17}$$

For previous experimental data, a continuous correlation for Nusselt number in heat transfer from cylinders to air in crossflow at $Re_c = 10^{-2}$-10^5 was proposed in (Fand and Keswani, 1972). If the variation of air thermal properties is not considered, the following expression is present (Fand and Keswani, 1972)

$$Nuc = 0.184 + 0.324Re_c^{0.5} + 0.291Re_c^{0.247+0.0407Re_c^{0.168}} \tag{18}$$

For experimental data available of convective heat transfer over a heated cylinder, an empirical formula was developed in (Zukauskas, 1972). If the variation of Prandtl number of air in the flow field is neglected, then the following correlation is written as

$$Nuc = 0.52Re_c^{0.5}Pr^{0.37} \tag{19}$$

For a single cylinder, the Nusselt number for heat transfer of crossflows proposed by (Whitaker, 1972) without viscosity variation reads as

$$Nuc = (0.4\sqrt{Re_c} + 0.06Re_c^{2/3})Pr^{0.4} \tag{20}$$

and the correlation developed in (Churchill and Bernstein, 1977) is written as

$$Nuc = 0.3 + \frac{0.62Re_c^{1/2}Pr^{1/3}}{[1 + (0.4/Pr)^{2/3}]^{1/4}}\left[1 + \left(\frac{Re_c}{28200}\right)^{5/8}\right]^{4/5} \tag{21}$$

For flows crossing in-line and staggered cylinder bundles, the correlation deduced in (Whitaker, 1972) is in the following form without consideration of viscosity variation

$$Nuc = (0.5\sqrt{Re_c} + 0.2Re_c^{2/3})Pr^{1/3} \tag{22}$$

It is shown that two correlations for single cylinder predict almost the same *Nuc*. *Nuc* predicted by CFD closes to but above *Nuc* that from five empirical correlations for single cylinder, suggesting the flow models and computational methods adopted seem proper and realistic. Furthermore, the natural convection heat transfer in the thermal chimney should be treated to be forced convection heat transfer. Since *Nuc* is still quite low, it needs to be enhanced by employing heat transfer enhancement methods in the future.

Based on Fig. 4(e), even though *Nur* is lower by approximate 1/3 than *Nuc*, the radiation effect still play an important role in forced convection heat transfer in the chimney and cannot be neglected.

3.3. Flow and temperature details

The air velocity vectors and velocity contours in eight cross-sections inside the chimney are illustrated in Fig. 5(top and middle rows). The air is sucked into the chimney with nearly uniform velocity and thin boundary layer at its inlet by buoyancy effect. Then it passes through the gaps between the heaters with the highest velocity as if a jet flow is generated. Once the air leaves from the gaps, the jets with the highest velocity mix rapidly with the air in the wake behind each heater and a core flow with thick boundary layer is formed gradually. Finally, the core flow is discharged from the chimney outlet. At a low heater nominal temperature, say $T_{hn} \leq 130$°C, the buoyancy effect is not so strong enough that the air flow is mainly confined in the central region of the chimney. As a result, dead air or boundary layer separated zones emerge in two corners of the chimney. As $T_{hn} > 130$°C, the dead air zones are shrunk quickly and disappear basically at $T_{hn} = 170$°C.

Additionally, upward air streams emerge outside the chimney, as shown in Fig. 5(bottom row). One stream flows into the chimney from its inlet and then out of the chimney, one stream flows upward along the walls outside the chimney. Eventually, it mixes with the air flow discharged from the chimney.

The velocity contours and vectors in the mid-span plane across the heaters are present at three heater nominal temperatures in Fig. 6. It is clearly shown that jet flows are established in the gaps between the heaters. Particularly, around the central heater (No.7 from the left) the strongest jet and the most significant large wake have occurred.

The air and chimney wall temperature contours in the mid-span plane cross the heaters inside the chimney at three heater nominal temperatures $T_{hn} = 90$, 130, 170°C are demonstrated in Fig. 7. The higher temperature zones in the air and chimney wall are basically ranged in the areas near the heaters at three heater nominal temperatures. At a lower nominal temperature, the higher temperature air zones can extend a long distance towards the downstream in comparison with that at a higher nominal temperature. This suggests that the primary heat exchanger should adopt new structures, namely multi-row heaters or the heaters with heat transfer enhancement elements to enhance its heat transfer effectiveness at a higher nominal temperature ($T_{hn} > 130$°C).

The higher temperature in the air body contacting with the chimney walls mainly occurs in the regions around the holes accommodating the heaters and two side walls close to heaters 1 and 12, respectively.

The thermal plume, which was found experimentally in (Lieberman and Gebhart, 1969; Kitamura et al., 1999; Chung et al., 2011) and numerically in (Ma et al., 2019; Kuehn and Goldstein, 1980; Saitoh et al., 1993; Lin et al., 2017; Grafsronningen and Jensen, 2017) in natural convection heat transfer around single horizontal cylinder heated as well as in steady laminar forced convection heat transfer from an unconfined cylinder presented in (Bharti et al., 1980) analytically, clearly exists downstream the cylinders in Fig. 7, especially at $T_{hn} = 130$, 170°C, but the plumes $T_{hn} = 90$°C are so wide that can merge with each other partially. The phenomenon agrees with the interferometric images of convection thermal field around two adjacently placed cylinders heated with the centre-to-centre distance of 2.5*d* made at wall temperatures 45, 50 and 60 °C in (Narayan et al., 2017).

The profiles of mean air temperature T_f and velocity u along flow path in the chimney are indicated in Fig. 8 at $T_{hn} = 90$, 130, 170°C, respectively. In Fig. 8(a), the velocities speed up towards the heaters, and experience a slight drop at the leading edge (front stagnation points), then show a dramatic increase until the narrowest part of the gap, subsequently find themselves in a very sharp drop towards the

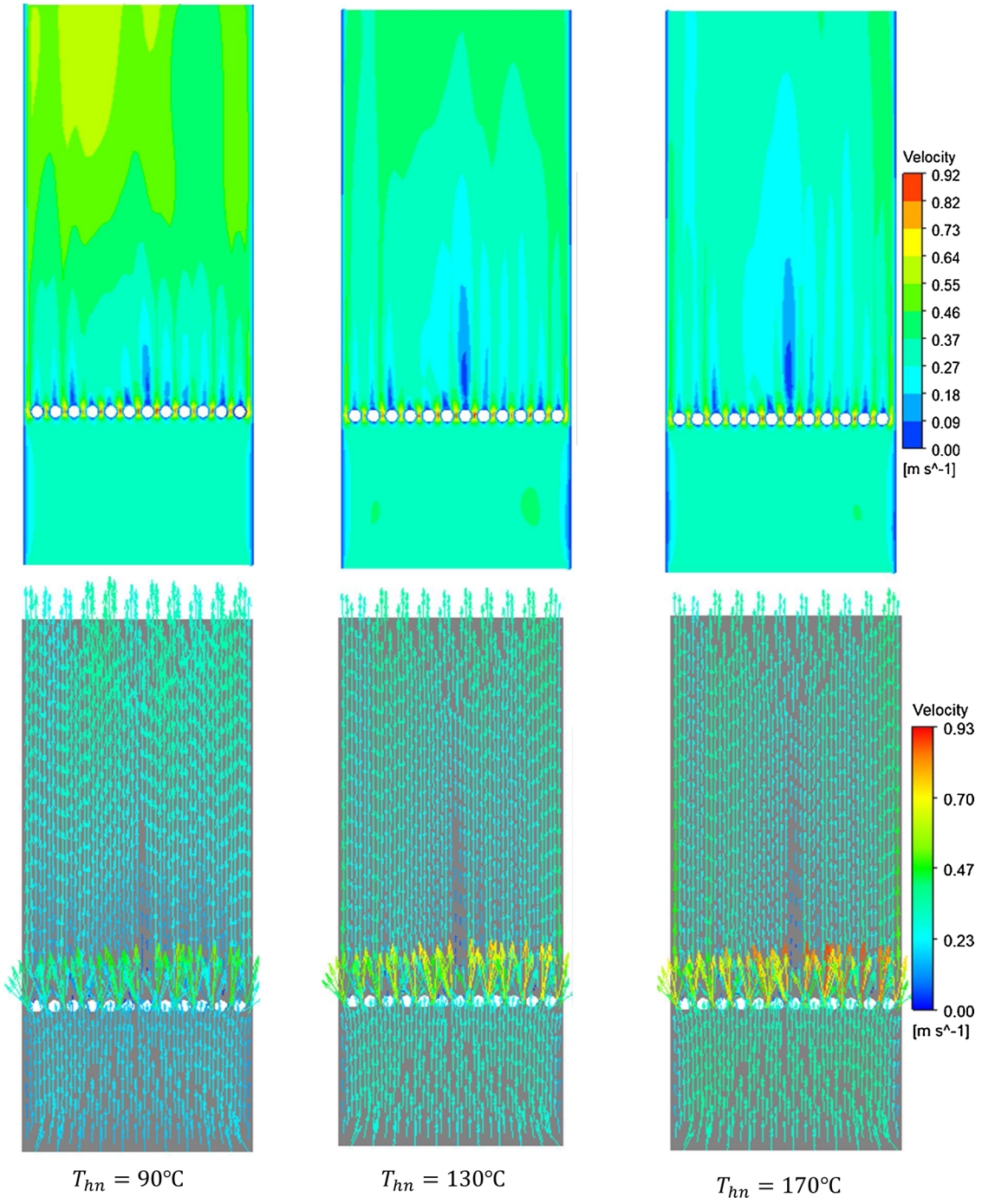

Fig. 6. The air velocity contours(top row) and vectors (bottom row) in the mid-span plane cross the heaters at three heater nominal temperatures T_{hn} = 90, 130, 170°C, respectively.

training edge(rear stagnation points), eventually maintain a recovery until the chimney outlet. The temperatures are subject to the similar variation profiles to the velocities, but don't vary so quickly as the latter do along the flow path.

The velocity and temperature profiles in the close-up region marked in Fig. 8(a) are localized and illustrated in Fig. 8(b). It is seen that the temperature profiles are nearly uniform in the gap between heaters at three nominal heater temperatures, and the higher the nominal temperature and the hotter the air in the gap. The highest velocity becomes fast with rising T_{hn}.

4. Discussion

In the paper, CFD simulations of conjugate heat transfer in a 3D thermal chimney have been launched to clarify the chimney thermal performance, and fluid flow and temperature details at various heater nominal temperatures ranged in (80–170) ℃ based on the steady RANS and $k-\omega$ turbulence model and variable heater surface temperature along its axis. Such work hasn't been documented in the literature so far, and it can be redeemed to be novel and original. The outcomes of the work can be meaningful for further concept design of outdoor thermal chimney in geothermal utilizations.

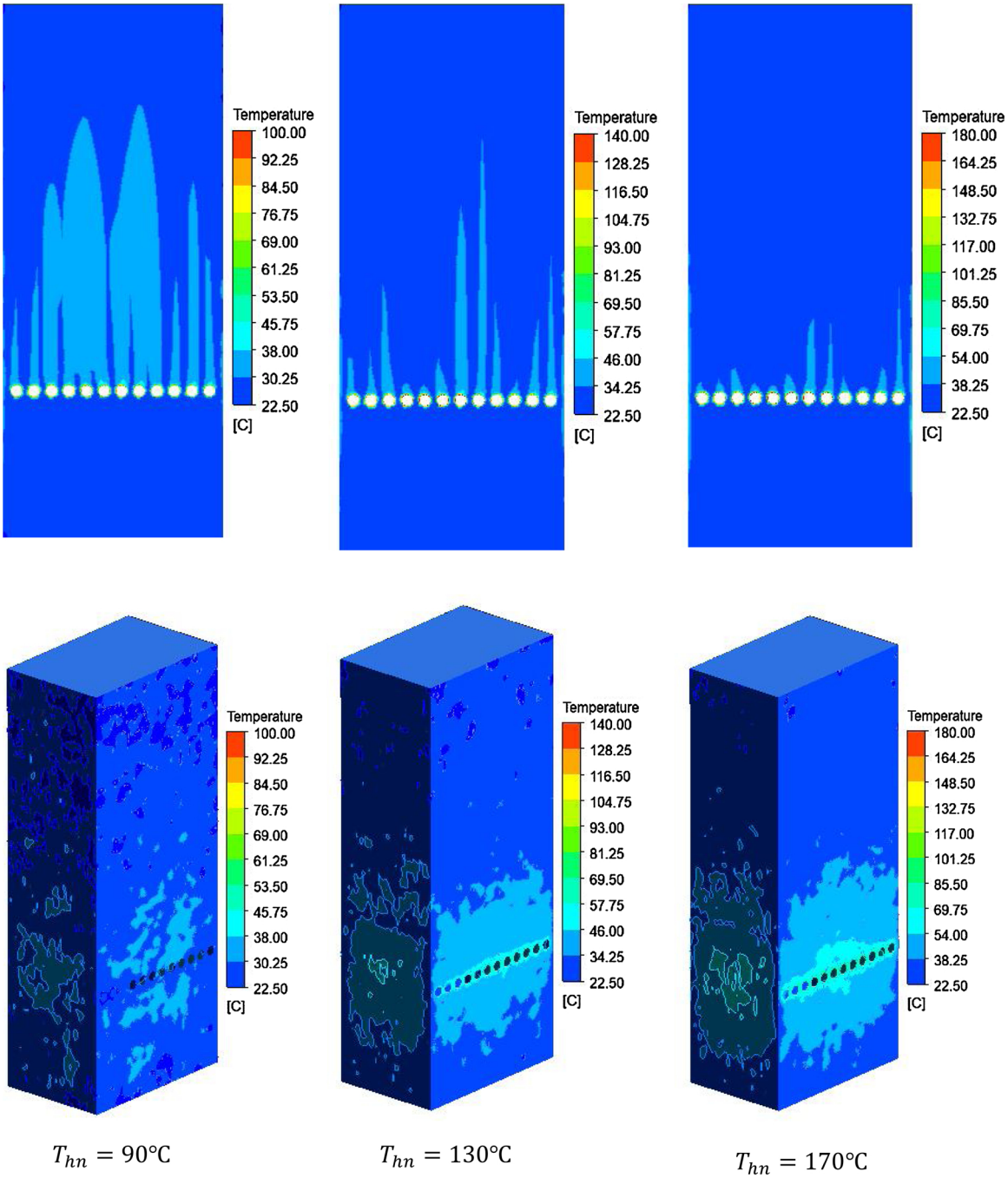

Fig. 7. The air and chimney wall temperature contours in the mid-span plane (top row) and the temperature contours in the air body (bottom row) inside the chimney at three heater nominal temperatures T_{hn} = 90, 130, 170°C, respectively, to identify temperature wakes behind the heaters three temperature scales are adopted.

4.1. Turbulence model validation

Since the standard $k-\varepsilon$ two equation turbulence model has been extensively applied in industrial turbulent flow simulations, and the $k-\omega$ based shear stress transport (SST) model is subject to a highly accurate prediction of the onset and the extent of flow separation (ANSYS Inc, 2011), they can potentially be involved in CFD simulations of conjugate heat transfer in the thermal chimney.

Convection Nusselt numbers from twelve heaters at 120°C heater nominal temperature predicted by using these turbulence models are displayed in Fig. 9. The Nusselt number *Nuc* estimated by the $k-\varepsilon$ model is lower than the number based on the empirical formula for single cylinder in (Whitaker, 1972) by half roughly. Therefore, the $k-\varepsilon$ model can result in a very underestimated convection Nusselt number and should be ruled out in CFD simulations of conjugate heat transfer in the thermal chimney.

The Nusselt numbers estimated by the SST model are equivalent to those predicted with the empirical expression for cylinder bundle in (Whitaker, 1972). Obviously, the SST model leads to an overestimated Nusselt number for the heaters in the thermal chimney. Hence, it should be careful for the model to be applied in CFD simulations of conjugate heat transfer in the thermal chimney.

The Nusselt numbers produced with the $k-\omega$ model are just above the curve of the empirical formula for single cylinder (Whitaker, 1972), suggesting this model is proper for CFD simulations of conjugate heat transfer in the thermal chimney in the paper.

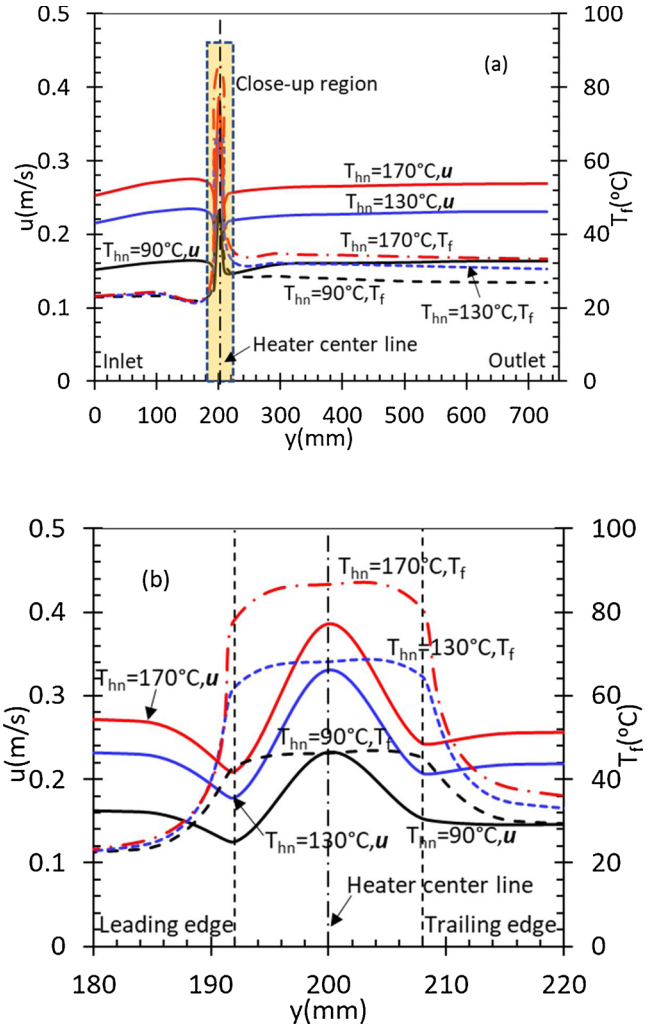

Fig. 8. The variations of mean air temperature T_f and velocity u along flow path in the chimney at heater nominal temperatures T_{hn} = 90, 130, 170℃, respectively, (b) is the curves in the zoomed area marked in (a).

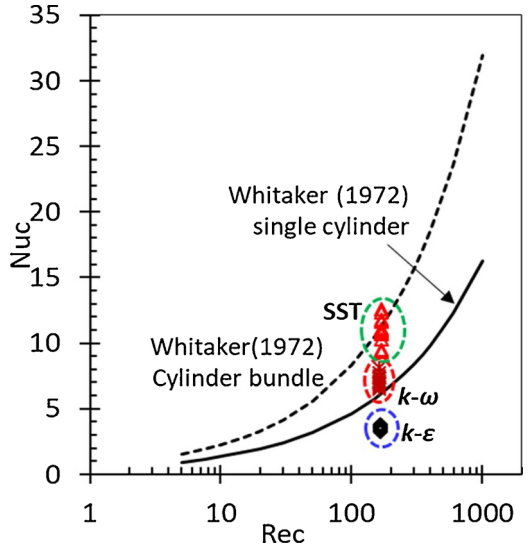

Fig. 9. The convection Nusselt numbers of twelve heaters at 120℃ heater nominal temperature predicted with the standard $k-\varepsilon$, $k-\omega$ and SST turbulence models, respectively, and compared with the correlations for single cylinder and cylinder bundle in (Whitaker, 1972).

4.2. Energy balance analysis

An energy balance analysis was performed at three heater nominal temperatures T_{hn} = 90, 130, 170℃, respectively, and the responding data are listed in Table 3. Most of the energy of the heaters, i.e. (39–51)%, depending on the heater temperature, is discharged from the chimney outlet, but (32-19)% energy is out of the chimney inlet, and (20–27)% energy is passed through the side walls, the rest less 10 % energy is lost from the heater ends. With increasing T_{hn} the energy loss percentages at the side walls and outlet are intensified, however, the percentages at the chimney inlet and other locations are decreased. The radiation loss, which is a percentage in (63–77) %, is much dominant at the chimney walls in comparison with that in the chimney inlet (0.3-0.4) % and outlet (2.3–3.9) %.

4.3. Effect of buoyancy on production and dissipation

In the simulations above, the buoyancy production P_{kb} in the k equation, and the buoyancy production term $P_{\omega b}$ in the ω equation have been disabled. To check their effects on the chimney thermal performance, air temperature rise and convection Nusselt number, they were activated with σ_b = 0.9 and C_3 = 1. It was found out that the energy gain coefficient, air temperature rise and Nusselt number were reduced by 0.016, 0.12 ℃ and 0.015 at T_{hn} = 130℃, for instance. The energy gain coefficient declination is essentially attributed to the slightly reduced air temperature rise and the quite large heat capacity 1005 J/(kg.K) of air. Obviously, the effect of buoyancy on turbulence production and dissipation can be ignored.

Note that the article is subject to a few limitations. Firstly, the proposed thermal chimney concept is with two exchangers, one is used as a heater and one serves as a condenser, as shown in Fig. 1. As the initial trial, the heater was involved only in our experiments and CFD simulations to examine if an air stream can be set up in a thermal chimney by the heater or not. If so, what the thermal performance of the chimney is and how the heat transfer and flow go on in the chimney. Additionally, this simplified chimney model can facilitate to develop appreciate experimental and analytical methods. In the followed work, an additional heat exchanger will be included.

Secondly, the chimney cross-section should be circular in outdoor application, however, the thermal chimney used in our experiments and simulations is with rectangular cross-section of constant area to facilitate chimney manufacturing. In the project, our principal purpose is to verify the concept design of thermal chimney proposed by us for freshwater production in geothermally sourced power plants, and subsequently to characterize the thermal performance, heat transfer and flow details for the chimney. The corresponding results can be meaningful to thermal design of the outdoor thermal chimney.

5. Conclusion

The conjugate heat transfer in a specifically designed thermal chimney with twelve electrical heaters was investigated by using CFD code-ANSYS 2019R CFX at various heater nominal temperatures based on steady 3D RANS equations and $k-\omega$ two-equation turbulence model as well as Boussinesq buoyancy assumption under 22.5 ℃ ambient temperature condition. The overall thermal performance of the chimney, heat transfer characteristics, temperature and flow fields in the chimney were clarified in detail. The radiation effect from the heaters to the air in the chimney was taken into account. The variable temperature profile on the heater surface along its axial direction was mapped, modelled and implemented as temperature boundary conditions with CEL in CFX-Pre. The flow field in the chimney was validated with our PIV measurements made in the mid-span plane cross the heaters at three heater nominal temperatures. The Nusselt number predicted was contrasted against existing correlations found in the literature. A few important issues associated with turbulence model,

Table 3
Energy balance analysis at three nominal heater temperatures.

Location	T_{hn} = 90°C		T_{hn} = 130°C		T_{hn} = 170°C	
	Power (W)	Percentage (%)	Power (W)	Percentage (%)	Power(W)	Percentage (%)
Side walls	18.89(14.55)	19.8(77.0)	52.01(34.68)	24.8(63.0)	86.93(54.74)	27.1(63.0)
Inlet	30.92(0.10)	32.4(0.3)	46.60(0.17)	22.2(0.4)	59.62(0.24)	18.5(0.4)
Outlet	37.27(1.47)	39.0(3.9)	99.10(2.77)	47.6(2.8)	163.82(3.82)	51.09(2.3)
Others	8.40	8.8	12.16	5.4	10.92	3.4
Total	95.49	100	209.87	100	321.29	100

The numerical figures in () are black body radiation power and its percentage.

effect of buoyancy on turbulence production and dissipation and energy balance analysis were addressed. It turned out that the heaters in the designed chimney can establish an air flow stream from its inlet to outlet by continuously heating the air inside the chimney. When the heater nominal temperature rises from 80 °C to 170 °C, the energy gain coefficient of the chimney increases to 0.60 from 0.40, but gets saturated after the nominal temperature is higher than 130 °C, the Reynolds number of the chimney varies from 2000 to 4000 in comparison with that of the heaters from 140 to 270, and the Nusselt number is just ranged from 7.0–8.2, which is slightly larger than the number predicted with five published correlations for heat transfer from cylinders to air in crossflow rather than free heat transfer from cylinders to stationary air in terms of Grashof number or Rayleigh number. The radiation from the heaters can make a (33–35)% contribution to the total heat transfer, and should not be neglected. When the nominal temperature is lower than 130 °C, the air separates from the chimney walls downstream the heaters, suggesting the heat exchanger operating temperature should not be below 130 °C. In forthcoming design of the chimney, useful measures should be developed to tackle both flow separation by optimizing chimney cross-sectional area profile and too low Nusselt number by involving heat transfer enhancement techniques. CFD simulations of a thermal chimney with two-row heaters/exchangers and high-resolution PIV measurements near the heaters and in cross-sections in the chimney are under way presently.

CRediT authorship contribution statement

Wenguang Li: Investigation, Methodology, Formal analysis, Visualization, Writing - original draft. **Guopeng Yu:** Investigation, Data curation, Methodology, Visualization. **Daniele Zagaglia:** Resources, Methodology, Validation. **Richard Green:** Resources, Supervision. **Zhibin Yu:** Conceptualization, Funding acquisition, Project administration, Writing - review & editing.

Declaration of Competing Interest

The authors declare that they have no known competing financial interests or personal relationships that could have appeared to influence the work reported in this paper.

Acknowledgement

The work was supported by EPSRC in the UK in terms of grants such as EP/N020472/1, EP/N005228/1, EP/P028829/1, EP/R003122/1 and EP/L024888/1 (National Wind Tunnel Facility), and the support was acknowledged indeed.

Appendix A. Analytical Temperature Profiles of Heaters

Initially, a thermal image was taken against 12 heaters by using a forward-looking infrared (FLIR) camera at 120 °C nominal temperature monitored by the thermal coupling fixed on the surface of heater 6, as seen in Fig. A1. Obviously, the temperature on the heater surface is non-uniform, but also varies from one heater to another. This fact suggests that non-uniform temperature should be assigned to each heater.

To develop non-uniform temperature profiles along the heater axis and across the heaters, further three experiments were performed by employing the FLIR camera at 120, 130 and 140 °C nominal temperatures under allowable working conditions for the camera. The FLIR A300 infrared camera was positioned on top of the chimney with the image sensor facing the upper surface of the heater row. Colour images were formed and transferred to real-time display on computer monitor. The images taken were digitized through FLIR ResearchIR software, and the temperature profiles along the axis of heaters 1, 3, 5, 7, 9 and 11 were extracted and modelled.

To establish analytical dimensionless temperature profiles, one-dimensional axial length coordinate system is generated for each heater, as shown in Fig. A1. The dimensionless length ξ is defined by the maximum axial length z_{min} and the minimum axial length z_{min} in such a way $\xi = (z - z_{min})/(z_{max} - z_{min})$.

Firstly, the experimental temperature data were best fitted by using fourth-order polynomial in terms of ξ to obtain an analytical temperature profile equation for each heater; the maximum temperature T_{hmax} was determined from these analytical temperature profile equations; the heater local temperatures were normalized by employing T_{hmax} for each heater; the mean of these maximum temperatures T_{hmaxm} was calculated across these heaters.

Secondly, all the dimensional local temperatures were put together and best fitted by using fourth-order polynomial in terms of ξ to decide the universal analytical expression of dimensionless temperature profile for all the heaters; meanwhile, the ratio T_{hmax}/T_{hmaxm} was best fitted with second-order polynomial against heater number i, and the fitting curves are compared with the corresponding experimental data in Fig. A2 at three nominal heater temperatures T_{hn}. It is demonstrated that the fourth-order polynomial regression for the local temperature profiles can achieve a coefficient of determination as high as 0.983 at least, suggesting a similar dimensionless temperature profile from one heater to another. The regression of second-order polynomial for T_{hmax}/T_{hmaxm} is satisfactory as well except the case at T_{hn} = 130 °C. Note that T_{hmax}/T_{hmaxm} values are small since they vary in the range of ± 2% only.

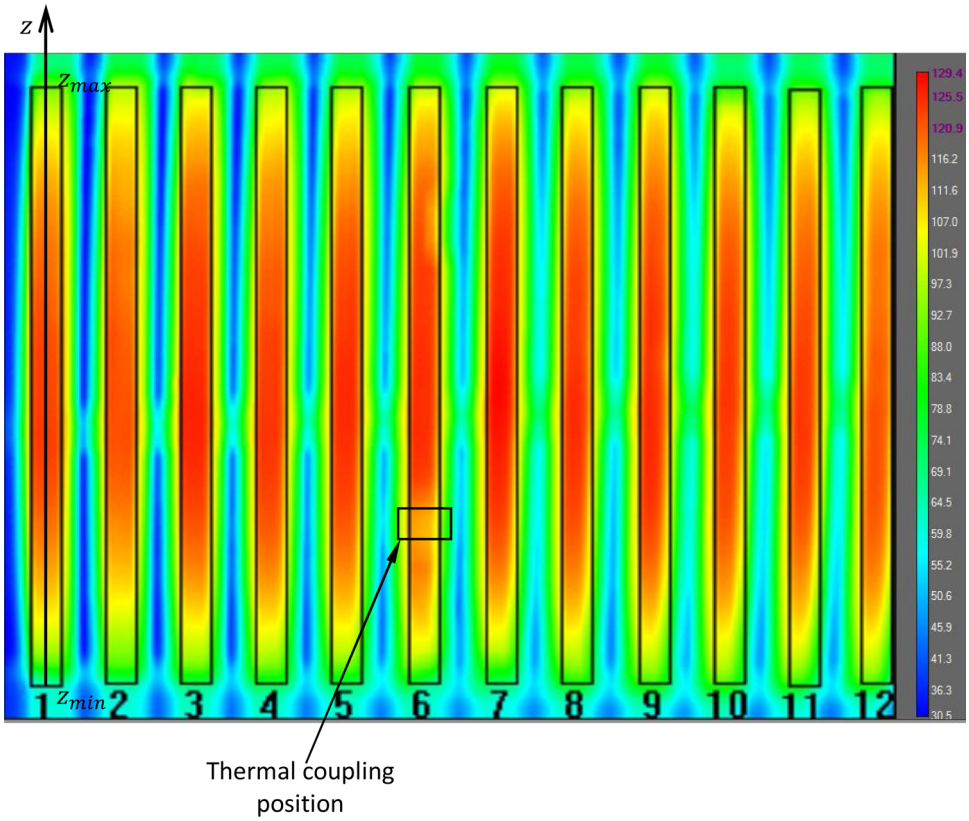

Fig. A1. A temperature image of heaters 1–12 taken by a forward-looking infrared camera at 120 ˚C nominal temperature monitored at the position marked on heater 6.

Finally, the relationship between T_{hmaxm} and T_{hn} was developed. A comparison of three universal temperature profiles is made in Fig. A3 along with the relationship between T_{hmaxm} and T_{hn}. There exists a similarity in the universal dimensionless temperature profiles in the range of $\xi \in [0.2,0.8]$ at T_{hn} = 120, 130 and 140 ˚C, however, beyond this region, the profile at T_{hn} = 130 ˚C falls off more than the rest. This fact implies that the experiment in the case of T_{hn} = 130 ˚C may involve some unpredicted errors somehow. Therefore, the correlations at T_{hn} = 130 ˚C have to be dismissed.

Based on the results fitted, the following analytical correlations are applied to assign the temperature on the heater surface according a known T_{hn} with CFX expression language (CEL)

$$T_{hmaxm} = 1.0732T_{hn} - 3.0218 \tag{23}$$

where the mean highest temperature on the surface of the heaters T_{hmaxm} is related to the highest temperature of each heater T_{hmax} such as

$$\begin{cases} \dfrac{T_{hmax}}{T_{hmaxm}} = -1.0885 \times 10^{-3}i^2 + 1.2486 \times 10^{-2}i + 0.9767, \ T_{hn} \le 130°C \\ \dfrac{T_{hmax}}{T_{hmaxm}} = -1.2214 \times 10^{-3}i^2 + 1.5562 \times 10^{-2}i + 0.\ 9605, \ T_{hn} > 130°C \end{cases} \tag{24}$$

in which i is heater number, i = 1,2, ..,12. The temperature profile T_h along each heater axis is calculated with T_{hmax} and ξ

$$\begin{cases} \dfrac{T_h}{T_{hmax}} = -1.6472\xi^4 + 3.1617\xi^3 - 2.5511\xi^2 + 1.0364\xi + 0.8262, \ T_{hn} \le 130°C \\ \dfrac{T_h}{T_{hmax}} = -1.9052\xi^4 + 3.6607\xi^3 - 2.8866\xi^2 + 1.1254\xi + 0.8193, \ T_{hn} > 130°C \end{cases} \tag{25}$$

The surfaces of 24 holes in two side walls of the thermal chimney need a temperature boundary condition. To fulfil this condition, the temperatures on these 5 mm wide surfaces are considered constant, their values are specified to be those at ξ = 0,1 in Eq. (25) simply.

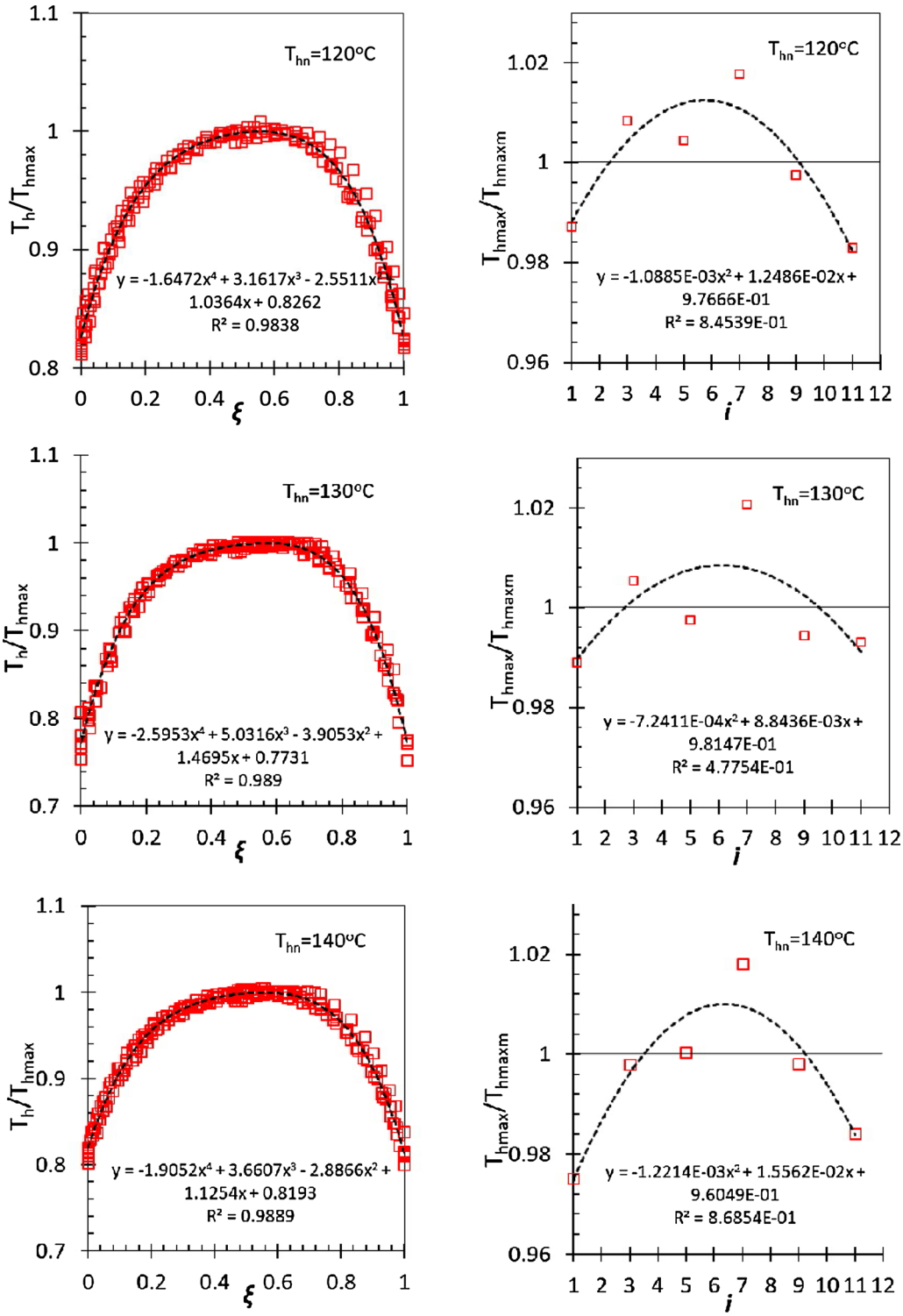

Fig. A2. The dimensionless experimental temperature profile T_h/T_{hmax} on the surfaces of heaters 1, 3, 5, 7, 9 and 11 along their dimensionless axial length ξ (left column), and dimensionless maximum temperature T_{hmax}/T_{hmaxm} on the surface on these heaters in terms of heater number i(right column).

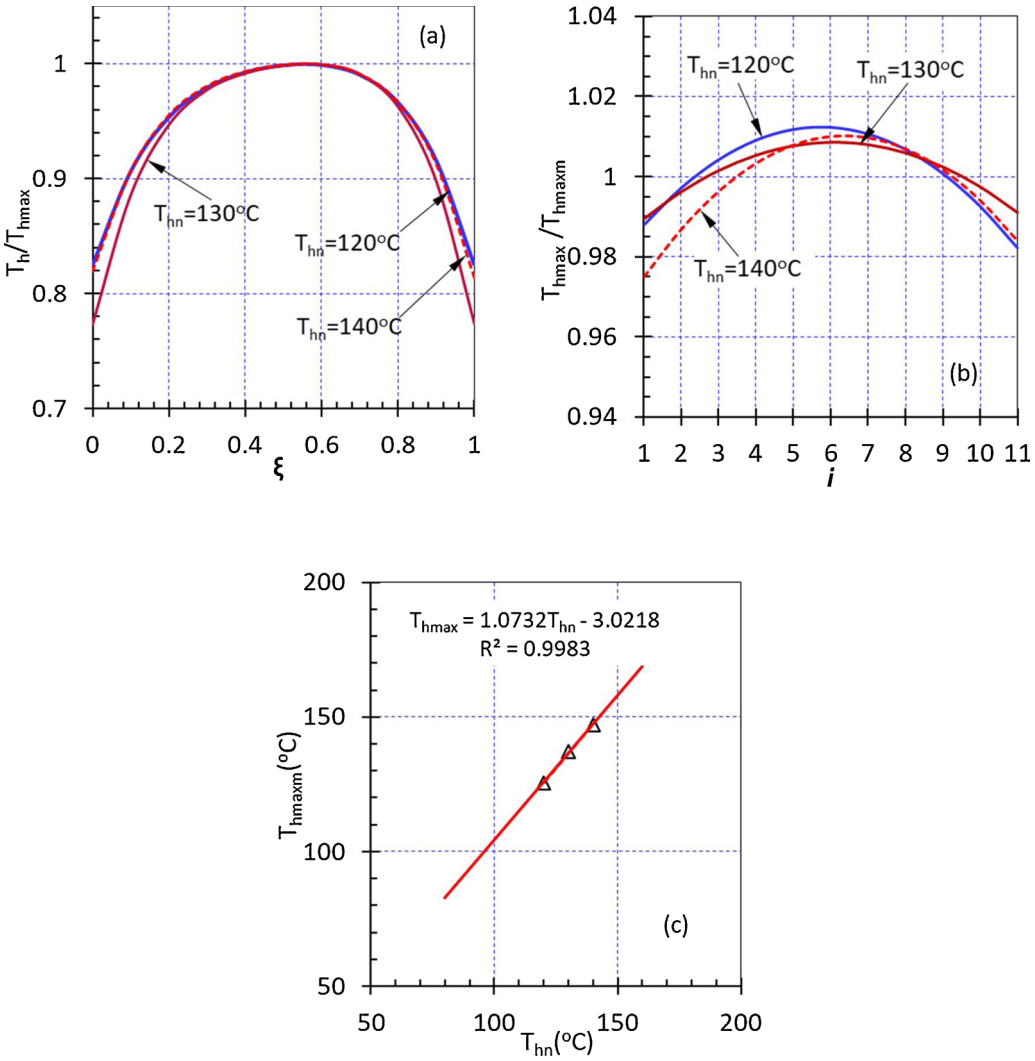

Fig. A3. A comparison of three analytical dimensionless temperature profiles (a), analytical dimensionless maximum temperature relationships (b), and the relation between the maximum temperature and the mean maximum temperature across these heaters (c).

Appendix B. Velocity Profile Validation with PIV

To validate the velocity profile, PIV measurements were performed in the mid-span plane cross the heaters in the chimney at three heater nominal temperatures T_{hn} = 80, 120, 160°C. The experimental set-up is shown in Fig. B1 (a). The chimney is located vertically in the middle of the isolated test section of a large wind tunnel which has enough space for air development under and above the chimney.

Flow field inside of the chimney is illuminated by the PIV laser and the field view is captured by high speed camera. The PIV laser light sheet was produced from the top to cover the mid-span plane of the chimney using a Nd: YAG laser capable of 100 mJ pulses of 8 ns duration at a maximum repetition rate of 200 Hz. The time delay between image pairs was set to be 0.5–2.2 ms. It needs to be adjusted according to different heater temperatures and velocity magnitudes within the chimney to appropriate resolve the velocity. The relationship between the chimney model co-ordinate system and camera coordinate system is well calibrated before recording. A 4 megapixel Phantom v341 digital video camera was used for PIV image recording, and 600 image pairs at a rate of 3 per second were taken for each experimental configuration. Post processing of the raw PIV images was completed using LaVison Davis 8 and MATLAB.

A typical velocity mapped by PIV at T_{hn} = 160°C is illustrated in Fig. B1 (b). In the figure, the dark colour indicates the regions where the correlations between two images are in failure due to significant noise in them, thus, the velocities are either missing or noisy at two horizontal lines with the distance y=-1d and 1d, hence these velocities have be ignored and will not be presented.

The air vertical velocities were extracted from PIV and CFD databases at four horizontal lines with the distances y=-5d, 5d, 10d and 20d to the heater centre line, as shown in Fig. B1 (b) and (c), where d = 16 mm is the heater outer diameter. These extracted velocities of both PIV and CFD are

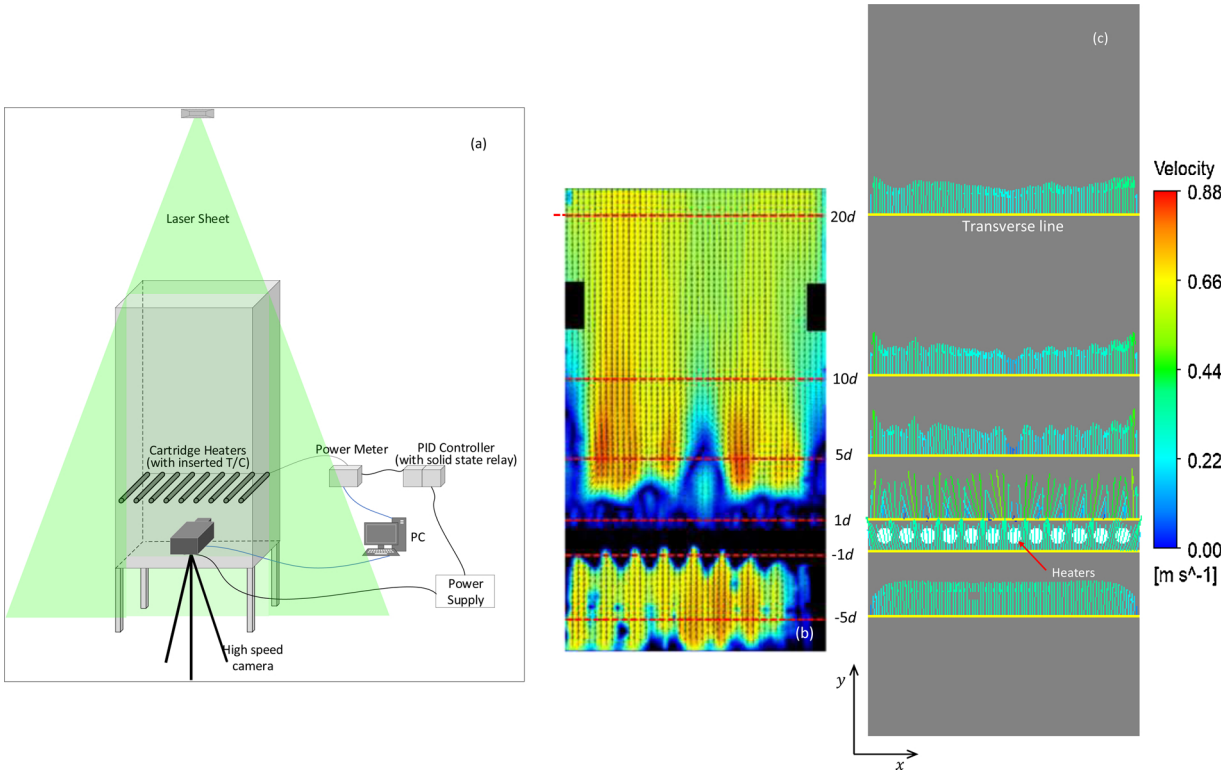

Fig. B1. The sketch of PIV experimental installation of the thermal chimney (a), a velocity vector plot in the mid-span plane cross the heaters measured by PIV at T_{hn} = 160℃ (b), and six transverse lines are marked with velocity vectors predicted by the CFD simulation at T_{hn} = 160℃ (c), the vertical velocity u_y is extracted from PIV measurements and compared with those in CFD simulations, d is the heater outer diameter.

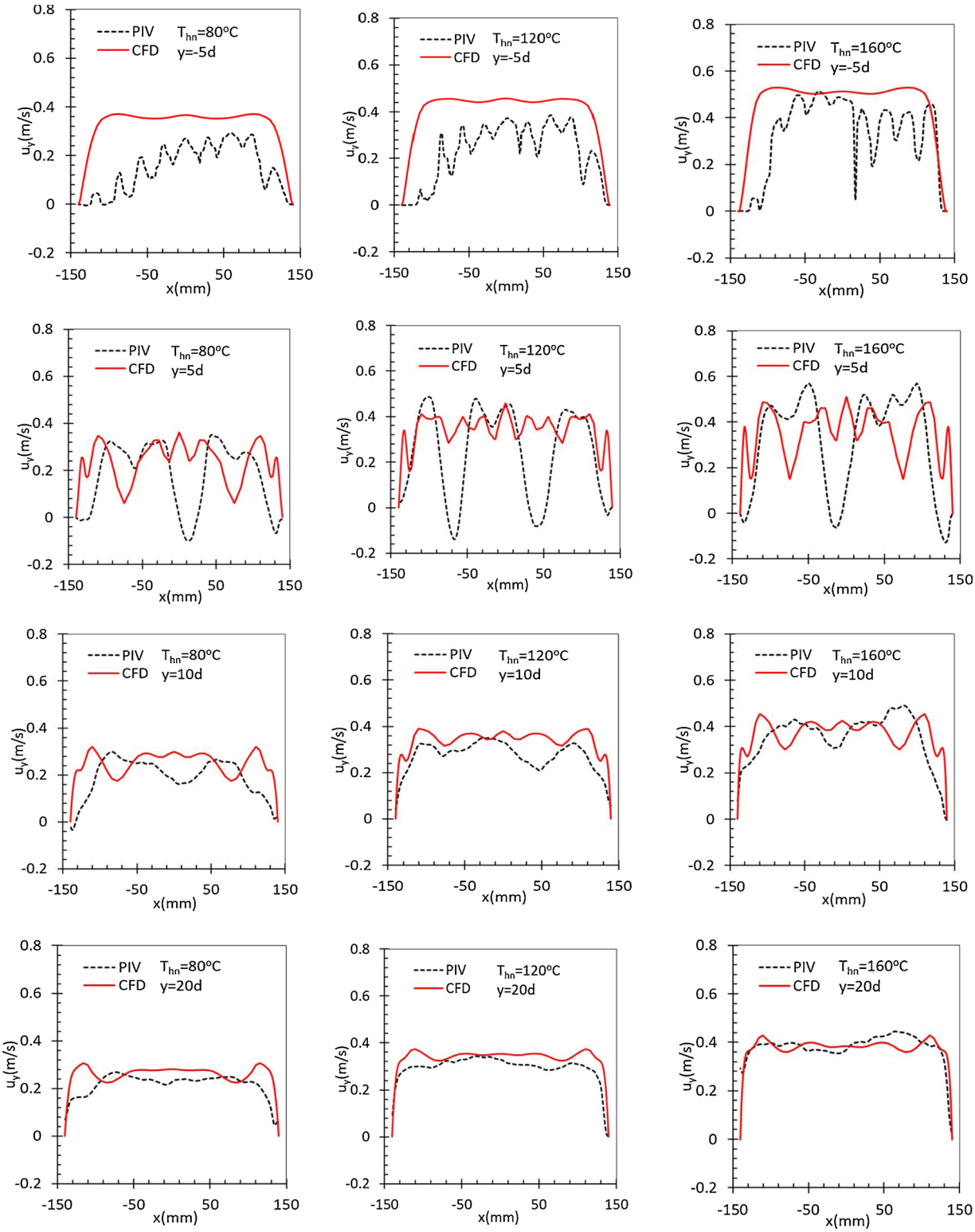

Fig. B2. A comparison of air vertical velocities between PIV and CFD on four transverse lines with the distances to the heater centre line of -5d, 5d, 10d and 20d in the mid-span plane cross the heaters at three heater nominal temperatures T_{hn} = 80, 120, 160°C, respectively.

contrasted in Figure B2.

At $y = -5d$ horizontal line (upstream near the heaters), because PIV leaser was shadowed by the heaters, the information about air velocity seems to be incomplete but also the velocity demonstrates a fluctuating and distorted profile, unlike the perfect velocity profile predicted by CFD. The distorted profile is caused from residual cross-wind in the test section of the wind tunnel.

At $y = 5d$ horizontal line (downstream near the heaters), the velocity profile in PIV becomes nearly symmetrical but with a few negative peaks at

Table B1
Errors in mean vertical velocity magnitude between PIV and CFD at three locations and three heater nominal temperatures.

T_{hn} (°C)	Mean u_y at 5d (m/s)			Mean u_y at 10d (m/s)			Mean u_y at 20d (m/s)		
	PIV	CFD	Error (%)	PIV	CFD	Error (%)	PIV	CFD	Error (%)
80	0.208	0.235	−13.0	0.204	0.248	−21.6	0.217	0.259	−14.6
120	0.258	0.341	−32.1	0.285	0.337	−18.2	0.306	0.335	−9.5
160	0.314	0.354	−12.7	0.354	0.370	−4.5	0.382	0.375	+1.8

Error = (PIV-CFD)/PIV × 100 %.

three nominal temperatures. In CFD velocity profiles, however, there are not any negative values at all. At $y = 10d$ and $20d$ horizontal lines (downstream far the heaters), the velocity profiles are similar between PIV and CFD.

In Table B1, the errors in the mean velocity between PIV and CFD at three nominal temperatures T_{hn} = 80,120,160°C are present. Roughly, the errors are in a range of (-30 ~ +2)%, depending on the nominal temperature.

References

Abdallah, A.S.H., Hiroshi, Y., Goto, T., et al., 2014. Parametric investigation of solar chimney with new cooling tower integrated in a single room for New Assiut city, Egypt climate. Int. J. Energy Environ. Eng. 5, 92. https://doi.org/10.1007/s40095-014-0092-6.

ANSYS Inc, 2011. CFX-Solver Theory Guide, Release 14.0. Southpointe, Canonsburg, USA, pp. 25–74.

Austin, A.L., Lundberg, A.W., 1975. A Comparison of Methods for Electric Power Generation From Geothermal Hot Water Deposits. ASME Paper 74-WA/Ener-10. .

Austin, A.L., Higgins, G.H., Howard, J.H., 1973. The Total Flow Concept for Recovery of Energy From Geothermal Hot Brine Deposits. Lawrence Livermore Laboratory Report UCRL-51366, April 3.

Bharti, R.P., Chhabra, R.P., Eswaran, V., 1980. A numerical study of the steady forced convection heat transfer from an unconfined circular cylinder. Heat Mass Transf. 23 (7), 971–979.

Chamorro, C.R., Mondejar, M.E., Ramos, R., et al., 2012. World geothermal power production status: energy, environmental and economic study of high enthalpy technologies. Energy 42, 10–18.

Chung, B.J., Eoh, J.H., Heo, J.H., 2011. Visualization of natural convection heat transfer on horizontal cylinders. Heat Mass Transf. 47 (11), 1445–1452.

Churchill, S.W., Bernstein, M., 1977. A correlating equation for forced convection from gases and liquids to a circular cylinder in cross-flow. ASME J. Heat Trans. 99 (2), 300–306.

Churchill, S.W., Chu, H.H.S., 1975. Correlating equations for laminar and turbulent free convection from a horizontal cylinder. Int. J. Heat Mass Trans. 18 (9), 1049–1053.

Cortez, D.H., Holt, B., Hutchinson, A.J.L., 1973. Advanced binary cycles for geothermal power generation. Energy Sources 1 (1), 73–94.

Fand, R.M., Keswani, K.K., 1972. A continuous correlation equation for heat transfer from cylinders to air in crossflow for Reynolds numbers from 10^{-2} to 2×10^{5}. Int. J. Heat Mass Transf. 15 (3), 559–565.

Fasel, H.F., Meng, F., Shams, E., et al., 2013. CFD analysis for solar chimney power plants. Sol. Energy 98, 12–22.

Ghorbani, B., Ghashami, M., Ashjaee, M., et al., 2015. Electricity production with low grade heat in thermal power plants by design improvement of hybrid dry cooling tower and a solar chimney concept. Energy Convers. Manage. 94, 1–11.

Grafsronningen, S., Jensen, A., 2017. Large eddy simulations of a buoyant plum above a heated horizontal cylinder at intermediate Rayleigh numbers. Int. J. Heat Mass Transf. 112 (5), 104–117.

Guan, Z., Gurgenci, H., 2009. Dry cooling technology in Chinese thermal power plants. Proceedings of Australian Geothermal Energy Conference 224–228.

Hassan, A., Ali, M., Waqas, A., 2018. Numerical investigation on performance of solar chimney power plant by varying collector slope and chimney diverging angle. Energy 142, 411–425.

Hilpert, R., 1933. Heat emission from heated wires and pipes in the air stream. Engineering Research 4 (5), 215–224.

Hooman, K., Huang, X., Jiang, F., 2017. Solar-enhanced air-cooled heat exchanger for geothermal power plants. Energies 10, 1676. https://doi.org/10.3390/en10101676.

Jameei, A., Akbarzadeh, P., Zolfaghazadeh, H., et al., 2019. Numerical study of the influence of geometric form of chimney on the performance of a solar updraft tower power plant. Energy Environ. 30 (4), 685–706.

Kitamura, K., Kamiiwa, F., Misumi, T., 1999. Heat transfer and fluid flow of natural convection around large horizontal cylinders. Int. J. Heat Mass Transf. 42 (22), 4093–4106.

Kuehn, T.H., Goldstein, R.J., 1980. Numerical solution to the Navier-Stokes equations for laminar natural convection about a horizontal isothermal circular cylinder. Int. J. Heat Mass Transf. 23 (7), 971–979.

Lal, S., Kaushik, S.C., Bhargav, P.K., 2013. Solar chimney: a sustainable approach for ventilation and building apace conditioning. Int. J. Dev. Sust. 2 (1), 277–297.

Lieberman, J., Gebhart, B., 1969. Interactions in natural convection from an array of heated elements, experimental. Int. J. Heat Trans. 12 (11), 1385–1396.

Lin, K.C., Bhosale, Y., Huang, C.Z., 2017. 3D-CFD investigation into free convection flow above a heated horizontal cylinder: comparison with experimental data. Appl. Therm. Eng. 120, 277–288.

Ma, H., He, L., Rane, S., 2019. Heat transfer-fluid flow interaction in natural convection around heated cylinder and its thermal chimney effect. In: Proceedings of the International Conference on Innovative Applied Energy, 14-15 March. Oxford, UK.

Maia, C.B., Ferreira, A.G., Valle, R.M., et al., 2009. Theoretical evaluation of the influence of geometric parameters and materials on the behaviour of the airflow in a solar chimney. Comput. Fluids 38 (3), 625–636.

Ming, T., de Richter, R.K., Meng, F., et al., 2013. Chimney shape numerical study for solar chimney power generating systems. Int. J. Energy Res. 37 (4), 310–322.

Narayan, S., Singh, A.K., Srivastava, A., 2017. Interferometric study of natural convection heat transfer phenomena around array of heated cylinders. Int. J. Heat Mass Transf. 109, 278–292.

Nasraoui, H., Driss, Z., Ayedi, A., et al., 2019. Numerical and experimental study of the aerothermal characteristics in solar chimney power plant with hyperbolic chimney shape. Arab. J. Sci. Eng. 44 (9), 7491–7504.

Park, D., Battaglia, F., 2015. Application of a wall-solar chimney for passive ventilation of dwellings. ASME J. Solar Energy Eng. 137 (6), 061006. https://doi.org/10.1115/1.4031537.

Pastohr, H., Kornadt, O., Gurlebeck, K., 2004. Numerical and analytical calculations of the temperature and flow field in the upwind power plant. Int. J. Energy Res. 28 (6), 495–510.

Saitoh, T., Sajiki, T., Maruhara, K., 1993. Bench mark solutions to natural convection heat transfer problem around a horizontal circular cylinder. Int. J. Heat Mass Transf. 36 (5), 1251–1259.

Saravanan, S., Sivaraj, C., 2013. Coupled thermal radiation and natural convection heat transfer in a cavity with a heated plate inside. Int. J. Heat Fluid Flow 40, 54–64.

Shati, A.K.A., Blakey, S.G., Beck, S.B.M., 2012. A dimensionless solution to radiation and turbulent natural convection in square and rectangular enclosures. J. Eng. Sci. Technol. 7 (2), 257–279.

Smith, I.K., 1993. Development of the trilateral flash cycles system Part 1: fundamental consideration, Proceedings of the Institution of Mechanical Engineers. Arch. Proc. Inst. Mech. Eng. Part A J. Power Energy 1990-1996 207 (3), 179–194.

Smith, I.K., da Silva, R.P.M., 1994. Development of the trilateral flash cycles system Part 2: increasing power output with working fluid mixtures, Proceedings of the Institution of Mechanical Engineers. Arch. Proc. Inst. Mech. Eng. Part A J. Power Energy 1990-1996 208 (2), 135–144.

Trusov, V., Kabakov, V., Sorokin, S., et al., 1995. Geothermal small power plants on the basis of application of total flow energy conversion. In: Proceedings of the World Geothermal Congress. Firenze, Italy.

Whitaker, S., 1972. Forced convection heat transfer correlations for flow in pipes, past flat plates, single cylinders, single spheres, and for flow in packed beds and tube bundles. Aiche J. 189 (12), 361–371.

Yu, G., Yu, Z., 2019. Combined power and freshwater generation driven by liquid-dominated geothermal sources. Energies 12, 1562. https://doi.org/10.3390/en12081562.

Zandian, A., Ashjaee, M., 2013. The thermal efficiency improvement of a steam Rankine cycle by innovative design of a hybrid cooling tower and a solar chimney concept. Renew. Energy 51, 465–473.

Zarrouk, S.J., Moon, H., 2014. Efficiency of geothermal power plants: a worldwide review. Geothermics 51, 142–153.

Zhai, X.Q., Song, Z.P., Wang, R.Z., 2011. A review for the applications of solar chimneys in buildings. Renew. Sust. Energy Rev. 15, 3757–3767.

Zhao, H., Yan, C., Sun, L., et al., 2015. Design of a natural draft air-cooled condenser and its heat transfer characteristics in the passive residual heat removal system for 10MW molten salt reactor experiment. Appl. Therm. Eng. 76, 423–434.

Zou, Z., Guan, Z., Gurgenci, H., et al., 2012. Solar enhanced natural draft cooling tower for geothermal power applications. Sol. Energy 86, 2686–2694.

Zukauskas, A., 1972. Heat transfer from tubes in crossflow. Adv. in Heat Trans. 18, 93–160.